JGR Solid Earth

RESEARCH ARTICLE
10.1029/2021JB021839

Petrogenesis of Himalayan Leucogranites: Perspective From a Combined Elemental and Fe-Sr-Nd Isotope Study

Qingshang Shi[1], Yongsheng He[1], Zhidan Zhao[1], Dong Liu[1], Nigel Harris[2], and Di-Cheng Zhu[1]

[1]State Key Laboratory of Geological Processes and Mineral Resources, China University of Geosciences, Beijing, China, [2]School of Environment, Earth and Ecosystem Sciences, Open University, Milton Keynes, UK

Key Points:

- The first integrated Fe-Sr-Nd isotopical and geochemical data set of Himalayan leucogranites and metasedimentary rocks are presented
- Isotopic and geochemical data suggest that two-mica and tourmaline leucogranites have not experienced a high degree of fractional crystallization
- The low δ^{56}Fe values of garnet leucogranites were likely derived from garnet accumulation

Supporting Information:

Supporting Information may be found in the online version of this article.

Correspondence to:

Y. He and Z. Zhao,
heys@cugb.edu.cn;
zdzhao@cugb.edu.cn

Citation:

Shi, Q., He, Y., Zhao, Z., Liu, D., Harris, N., & Zhu, D.-C. (2021). Petrogenesis of Himalayan leucogranites: Perspective from a combined elemental and Fe-Sr-Nd isotope study. *Journal of Geophysical Research: Solid Earth*, *126*, e2021JB021839. https://doi.org/10.1029/2021JB021839

Received 4 FEB 2021
Accepted 21 JUL 2021

Abstract The petrogenesis of Himalayan leucogranites remains crucial for understanding the thermal and tectonic evolution of the Himalayan orogen. To understand whether they are largely pristine melts of crustal anatexis or have experienced a high degree of fractional crystallization (FC), we present Fe isotopic data of 30 representative Himalayan leucogranites and 9 local metasedimentary rocks. Excepting three garnet leucogranites with low δ^{56}Fe (−0.04‰–0.06‰) that are likely affected by garnet accumulation, tourmaline, and two-mica leucogranites have largely homogeneous δ^{56}Fe from 0.13‰ to 0.24‰ irrespective of their highly variable SiO_2, MgO, and FeOt contents. Combined with observed mineral assemblages and available fractionation factors, this does not support a high degree of FC (with or without assimilation) in their petrogenesis. The elevated δ^{56}Fe relative to the supposed source rocks, represented by metasedimentary rocks and/or metabasite with a δ^{56}Fe value of 0.10‰, by ~0.07‰, may reflect Fe isotope fractionation during crustal anatexis. This study indicates most leucogranites can provide robust constraints on the conditions of crustal anatexis and thus the thermal and tectonic evolution of the Himalayan orogen.

Plain Language Summary The Himalayas have been formed from the collision between two tectonic plates. During their formation, the rocks of the continental crust have melted to form leucogranites which potentially provide important information on how the collision process evolves. Several recent studies of rare-element mineralization associated with these granites have argued that the magmas result from extensive removal of early formed minerals during the cooling of the magma (fractional crystallization [FC]) which, if true, would undermine their usefulness as monitors of the collisional process. In this study, we address this issue through a geochemical approach that combines isotopic data from iron, strontium, and neodymium. Whereas Sr and Nd give information on the source of the magmas, the isotopes of Fe will remain largely unfractionated if the granites result simply from melting the crust but fractionate significantly during FC. Our results reveal very limited fractionation of Fe isotopic compositions for two types of leucogranites, which is inconsistent with the model requiring a high degree of FC but supports the interpretation that they represent largely unfractionated crustal melts. Our study therefore confirms that Himalayan leucogranites can provide reliable probes for the thermal and tectonic evolution of the Himalayan crust.

1. Introduction

Himalayan leucogranites are silica-rich and strongly peraluminous; they have been widely proposed to be primary melts of crustal anatexis, given their compositions comparable to experimental melts of local meta-sediments and crustal radiogenic (Sr-Nd-Pb-Hf) and stable isotopic (H-O-Si) compositions (Deniel et al., 1987; France-Lanord et al., 1988; Hopkinson et al., 2017; X.-C. Liu et al., 2018; Patiño Douce & Harris, 1998). Their petrological and geochemical variations were considered to be derived from different melting mechanisms, for example, dehydration melting or fluid-present melting of a single source (metapelite) or multiple sources (metapelite and metagraywacke or amphibolite) under different P - T - X_{H_2O} conditions (Guillot & Le Fort, 1995; Inger & Harris, 1993; Knesel & Davidson, 2002; Le Fort, 1975; Patiño Douce & Harris, 1998; Zeng, Gao, & Xie, 2011). For example, at high pressure (~1 GPa), fluid-present melting of muscovite would generate leucogranite melts with high Na/K and CaO contents (L.-E. Gao et al., 2017; Patiño Douce & Harris, 1998; Zhang et al., 2004). However, at low pressure (~6 kbar), muscovite dehydration melting would generate leucogranite melts with high Rb/Sr and low Na/K, Sr, and Ba contents (Harris

& Inger, 1992; Patiño Douce & Harris, 1998). More enriched Sr-Nd-Hf isotopes in some Himalayan intrusions suggest that the melting source contains a contribution from the Lesser Himalayan sequence (Guo & Wilson, 2012; Hopkinson et al., 2019). Some leucogranites in southern Tibet with high Sr/Y ratios and relatively depleted Sr-Nd isotopic compositions indicate partial melting of amphibolite under thickened crustal conditions (Ji et al., 2020; Z.-C. Liu et al., 2014; Zeng, Gao, & Xie, 2011; Zeng, Gao, Xie, & Liu-Zeng, 2011; Zeng et al., 2019). Thus, the Himalayan leucogranites have been used to reflect the P - T - X_{H_2O} conditions and the tectonic evolution of Himalayan orogenic belt (Aikman et al., 2008; Gao & Zeng, 2014; Hopkinson et al., 2019; Huang et al., 2017; Weinberg, 2016).

In contrast, the chemical variation of Himalayan leucogranites has been considered by some recent studies to result from late differentiation (Z.-C. Liu et al., 2014, 2019; R. Wang et al., 2017; F.-Y. Wu et al., 2020). Overall, most Himalayan leucogranites have strong negative Eu anomalies, low Zr/Hf and Nb/Ta ratios as well as a strong rare earth element tetrad effect that evolves with decreasing zircon saturation temperatures (F. Wu et al., 2017; F.-Y. Wu et al., 2020). However, these geochemical characteristics are equally consistent with varying melt fractions from sedimentary sources, an interpretation supported by petrographic evidence which precludes the fractional crystallization (FC) of feldspars in leucogranite petrogenesis (Inger & Harris, 1993). Given their highly evolved compositions and recently documented rare-metal mineralization, the leucogranites from Xiaru, Ramba, and Cuonadong plutons have been termed as highly fractionated granites (Z.-C. Liu et al., 2014, 2016; Xie et al., 2019). Accordingly, it has been proposed that most Himalayan leucogranites were generated by extreme degree of FC (e.g., four stages of 75% fractionation; F.-Y. Wu et al., 2020). As highly fractionated granites, the characteristics of primary magmas for Himalayan leucogranites are difficult to constrain (e.g., Z.-C. Liu et al., 2016). Accordingly, previous conclusions on the thermal and tectonic evolution of Himalayan orogenic belt based on leucogranites may need reconsideration. Therefore, it is crucial to elucidate whether Himalayan leucogranites were generated by extreme magma differentiation or directly by crustal anatexis. This dilemma, however, is difficult to resolve, since both petrogenesis models can explain the mineral assemblage and chemical composition of Himalayan leucogranites (e.g., Fan et al., 2021; P. Gao et al., 2016; F. Wu et al., 2017).

An iron (Fe) isotopic study could resolve this dilemma and shed new light on the petrogenesis of Himalayan leucogranites, since Fe isotopes fractionate significantly during granitic magmatism (e.g., δ^{56}Fe from 0.08‰ to 0.64‰ for granites with SiO_2 > 71 wt% in Du et al., 2017; Foden et al., 2015; He et al., 2017; Heimann et al., 2008; H. Wu et al., 2017 and Xia et al., 2017). Fe isotopic fractionation during granitic magmatism is regulated by the redox and chemical composition of the melt and co-existing mineral assemblages (Dauphas et al., 2014; He et al., 2017; Sossi & O'Neill, 2017). Phases hosting Fe with higher charge and lower coordination number prefer heavier isotopes. Mafic silicate minerals (e.g., biotite and amphibole) enriched in ferrous Fe are isotopically lighter, while magnetite ($Fe^{3+}/\sum Fe = 0.69$) is isotopically heavier than coexisting granitic melts with low (Na + K)/(Ca + Mg) (Heimann et al., 2008; Sossi & O'Neill, 2017; Telus et al., 2012; H. Wu et al., 2017). With increasing (Na + K)/(Ca + Mg) in the melt, its Fe isotopes can be heavier than magnetite in turn (Dauphas et al., 2014; He et al., 2017). The δ^{56}Fe of granites directly generated by crustal anatexis deviate from their source rocks by a limited extent, that is, less than $\Delta^{56}Fe_{melt\text{-}residua}$, exemplified by migmatites from Black Hills and the Dabie orogen where the apparent Fe isotope fractionation between leucosomes and melanosomes is about 0.10‰ (Telus et al., 2012; L.-J. Xu et al., 2017). On the contrary, Fe isotope fractionation can become much larger during extreme FC of granitic melts, for example, elevating the melt δ^{56}Fe by >0.5‰ (Dauphas et al., 2014; Du et al., 2017). This difference is because crustal anatexis is a batch process while FC is a Rayleigh process.

To better understand their petrogenesis, here, we report combined elemental and Fe-Sr-Nd isotopic data for 30 Himalayan leucogranites. We also measured nine metasedimentary samples from the Greater Himalayan Sequence, which represent the possible source of Himalayan leucogranites (Inger & Harris, 1993; Patiño Douce & Harris, 1998). The mineral separates from five selected leucogranite samples were also measured, because tourmaline, an important Fe hosting mineral in the leucogranite, has not been well investigated for Fe isotopes hitherto. Based on new constraints from Fe isotopic data, the role of partial melting and extreme FC has been investigated in Himalayan leucogranites.

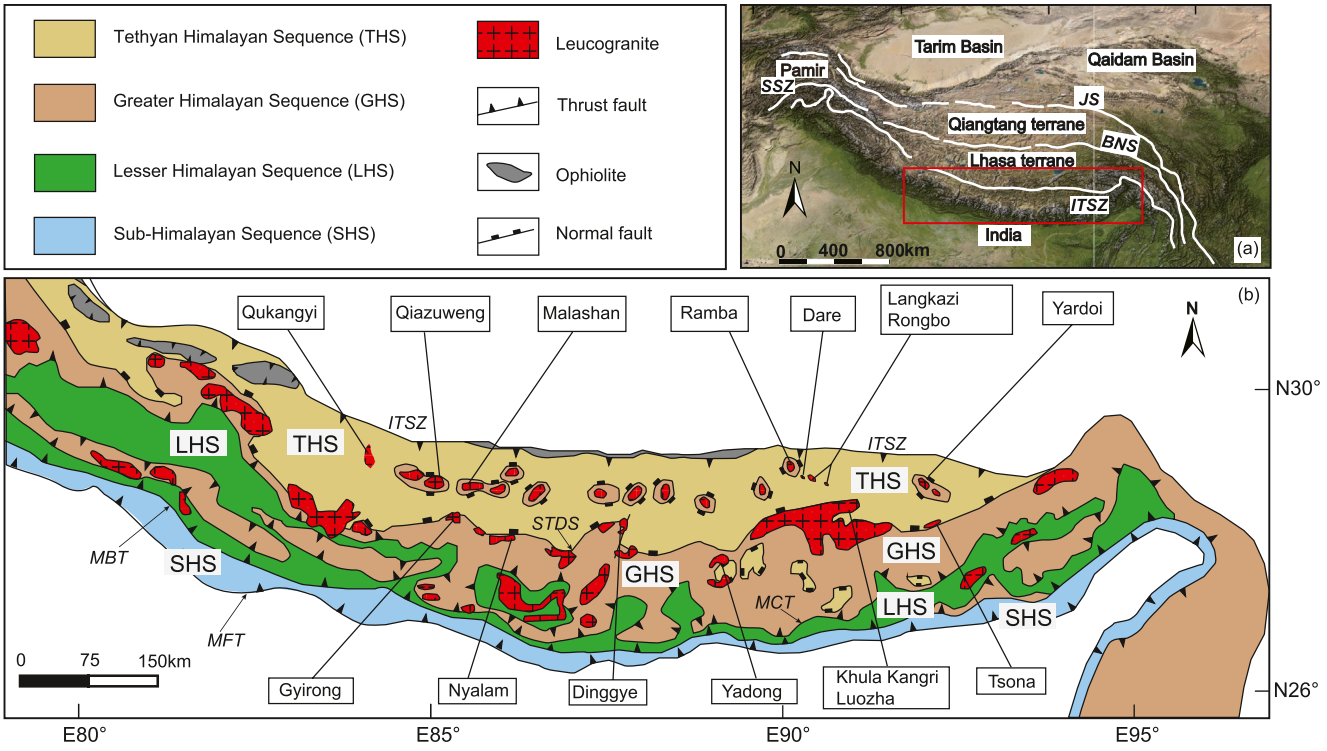

Figure 1. Simplified geological map of the Himalayan orogen (modified after Z. Xu et al., 2013). Leucogranite plutons measured in this study are labeled. JS, Jinsha suture zones; BNS, Bangong Nujiang suture zone; SSZ, Shyok suture zone; ITSZ, Indus-Tsangpo suture zone; STDS, Southern Tibetan Detachment System; MCT, Main Central Thrust; MBT, Main Boundary Thrust; MFT, Main Frontal Thrust.

2. Geological Background and Sample Description

The Himalayan orogen is a consequence of the ongoing continental collision between India and Asia since the Paleogene (Figure 1) (Ding et al., 2005; Hodges, 2000; X. Hu et al., 2016; Yin & Harrison, 2000; D. C. Zhu et al., 2015). It is divided into four lithotectonic units: (a) the Tethyan Himalayan Sequence, bounded by the Indus-Tsangpo suture to the north and the Southern Tibetan Detachment System to the south and mainly composed of very low to low-grade Neoproterozoic to Eocene marine sediments; (b) the Greater Himalayan Sequence, lying tectonically below the Tethyan Himalayan Sequence and mainly comprised of medium to high grade metasedimentary and meta-igneous rocks; (c) the Lesser Himalayan Sequence, bounded by the Main Central Thrust at the top and the Main Boundary Thrust at the bottom and made up of very-low grade to lower amphibolite facies metamorphic rocks with an age range of 1870–850 Ma; and (d) the sub-Himalayan Sequence, as the lowermost tectonic unit, mainly composed of Neogene sediments deposited in the active Himalayan foreland basin (Carosi et al., 2018; Kohn, 2014; Yin, 2006). Two roughly parallel granite belts are identified due to their temporal and spatial differences in the Himalayan orogen (Yin & Harrison, 2000). The southern one is the High Himalayan granite belt and consists of Oligocene-Miocene granite dikes, sills, and plutons intruded into the Greater Himalayan Sequence along with the Southern Tibetan Detachment System (Weinberg, 2016; F. Wu et al., 2015). The northern one is the Tethyan Himalayan granite or North Himalayan granite belt which intrudes into the Tethyan Himalayan Sequence as the North Himalayan Gneiss Dome (Zeng, Gao, Xie, & Liu-Zeng, 2011).

Thirty Himalayan leucogranites and nine metasedimentary rocks were collected in this study (Figure 1, Tables S1 and S2), and the latter represent the exposed counterparts of source rocks for the former. The leucogranite samples can be divided into three types based on their petrology: two-mica, tourmaline, and garnet leucogranites, which represent the major magmatic stage. The aplite, pegmatite, and hydrothermal alteration granite which represent the magmatic-hydrothermal and hydrothermal stages, were not considered here, given the potential complex modification on whole-rock δ^{56}Fe during hydrothermal processes (e.g., Markl et al., 2006; Y. Wang et al., 2011; B. Zhu et al., 2016). The two-mica leucogranites are composed

of biotite, muscovite, feldspars, and quartz. The other two types of leucogranites contain characteristic tourmaline and garnet instead of biotite respectively, except for sample YD1306. This sample, as a tourmaline leucogranite, also contains trace biotite. A detailed petrological description is given in Table S1. All leucogranite samples were collected distal from the pluton boundary without xenoliths and are recovered from both the Tethyan and High Himalayan granite belts (Figure 1). Metasedimentary samples were collected from the kyanite zone to the sillimanite zone of Greater Himalayan Sequence in central Nepal and Bhutan. They range from schist to gneiss with the key pelitic mineral assemblages of muscovite ± biotite ± garnet ± kyanite ± sillimanite (Table S2). The muscovite-garnet schist (Sample N13) has been used as the starting material of melting experiments that succeeded in generating melts of Himalayan leucogranite compositions (Patiño Douce & Harris, 1998).

3. Analytical Methods

All the samples were thoroughly cleaned, and the weathered surface layers were removed before crushing in a corundum jaw crusher to 60 mesh. Subsequently, the samples were powdered in an agate ring mill to 200 mesh. Whole-rock major and trace elements were measured at the State Key Laboratory of Geological Processes and Mineral Resources (GPMR), Wuhan. Sample powders were mixed with $Li_2B_4O_7$, LiBr, and NH_4NO_3, and fused in a Pt crucible. Major elemental data were obtained on the prepared glasses using X-ray fluorescence spectrometry (Shimadzu XRF-1800). Loss on ignition (LOI) was measured gravimetrically (Table S3). Accuracy is better than 3% (Ma et al., 2012). For trace elements analysis, 50 mg whole-rock powders were dissolved by HF + HNO_3 in Teflon bombs, and then sealed at 190°C for 48 h. The samples were dried, dissolved in 100 g 2% HNO_3, and then measured by Agilent 7500a (Table S3). The detailed analytical procedures have been previously reported (Y. Liu et al., 2008). The accuracy is routinely better than 5% for the reported trace elements, which is confirmed by analyses of international rock standards (Table S4). The FeO contents were measured by redox titration using $K_2Cr_2O_7$ solution at the China University of Geosciences, Beijing, and $Fe^{3+}/\Sigma Fe$ was calculated accordingly (i.e., (FeOt − FeO)/FeOt). The accuracy is <10% for the obtained $Fe^{3+}/\Sigma Fe$ (He et al., 2017). Mineral separation was handpicked under a binocular microscope from coarsely crushed samples (80–120 mesh).

Whole-rock powders for Sr-Nd isotopes were dissolved in the clean Teflon bombs with HF + HNO_3 + $HClO_4$, and then chemical separations were performed using conventional ion exchange procedures. Sr and Nd isotopes were analyzed using a Thermo-Finnigan TRITON thermal ionization mass spectrometer (TIMS) at the Tianjin Institute of Geology and Mineral Resources following the procedure by D. Liu et al. (2017). Sr and Nd isotopic ratios were corrected for instrumental fractionation by normalization against $^{86}Sr/^{88}Sr = 0.1194$ and $^{146}Nd/^{144}Nd = 0.7219$, respectively (Table S5). Repeated analyses of Sr standards BCR-2 and NBS987 yielded average $^{87}Sr/^{86}Sr$ ratios of 0.704975 ± 0.000021 (2σ, $n = 6$) and 0.710218 ± 0.000005 (2σ, $n = 7$), respectively. The average $^{143}Nd/^{144}Nd$ values of BCR-2 and a laboratory internal standard solution (LRIG-Nd) are 0.512635 ± 0.000004 (2σ, $n = 7$) and 0.512201 ± 0.000003 (2σ, $n = 8$), which agrees well with the recommended values (C.-F. Li et al., 2007).

Iron isotope analyses were conducted at the Isotope Geochemistry Laboratory, China University of Geosciences, Beijing, following the procedures previously established (Dauphas, Pourmand, & Teng, 2009; He et al., 2015; C. Zhu et al., 2018). Approximately 3–35 mg whole-rock powders were dissolved in a 3:1 mixture of concentrated HF-HNO_3 in Teflon beakers on a hotplate at ~130°C until the solutions became transparent. After evaporation to dryness at 140°C, the residues were refluxed subsequently with aqua regia (HCl: HNO_3 = 3:1) and excess HNO_3 aqua regia (HCl: HNO_3 = 2:1) at 130°C for two times. The samples were dissolved in 6 N HCl before chromatographic purification. Iron was separated from matrix elements and potential isobars with 1 ml AG1-X8 pre-clean resin in an HCl medium. Whole procedure blank is less than 10 ng for Fe and thus can be considered negligible compared to >50 μg sample Fe processed. Fe isotopic ratios were analyzed on a Neptune Plus multiple collector inductively coupled plasma mass spectrometer (MC-ICP-MS) on high-resolution modes, with mass bias corrected by the sample-standard bracketing method. The Fe isotopic data are reported in δ values relative to IRMM-014 ($\delta^i Fe$ (‰) = $[(^iFe/^{54}Fe)_{sample}/(^iFe/^{54}Fe)_{IRMM\text{-}014} - 1] \times 1000$, where i can be 56 or 57). The isotopic measurement sequence for each sample Fe solution was repeated four times, and the mean values are reported. The internal uncertainties are given as 2SE after Dauphas, Pourmand, and Teng (2009) and He et al. (2015), considering the errors arising from both the

chemical procedures and the MC-ICP-MS measurement, which are typically ≤0.05‰ for δ^{56}Fe (Table S6). Both the long-term reproducibility and accuracy are better than 0.05‰ for δ^{56}Fe, which comes from the duplicate measurements on 24 geological standards over 7 years (He et al., 2015; C. Zhu et al., 2018). The USGS standard AGV-2 and GSP-2 were processed with unknown samples, yielding values (δ^{56}Fe = 0.09 ± 0.04‰ and 0.15 ± 0.04‰, respectively) consistent with the previously published values within quoted uncertainties (e.g., Craddock & Dauphas, 2011; Dauphas, Craddock, et al., 2009; He et al., 2015; Sossi et al., 2012). Duplicate analyses of samples, independent from sample dissolution to instrument analysis, also show consistent results within quoted errors (Table S6).

4. Results

The Himalayan leucogranites show large geochemical variation, especially for two-mica leucogranites which can be divided into high Sr/Y and low Sr/Y groups, based on their Sr and Y contents and Sr-Nd isotopic distinction (Figures 2a and 3). The low Sr/Y two-mica leucogranites have high SiO_2 (70.80–76.26 wt%) and Al_2O_3 (12.49–15.69 wt%) and low MgO (0.16–0.94 wt%), TiO_2 (0.09–0.33 wt%), and (Na + K)/(Ca + Mg) (2.94–15.23) values (Figure 2). They show high Rb (181–398 ppm) and varied Sr (35–262 ppm), Y (5.52–45.18 ppm), and Ba (52–615 ppm) contents, with Rb/Sr and Sr/Y ratios ranging from 0.80 to 7.32 and 0.77 to 22.39, respectively. Compared to the low Sr/Y two-mica leucogranites, the high Sr/Y two-mica leucogranites show lower Rb (84–277 ppm) and Y (2.19–8.30 ppm) and higher Sr (157–801 ppm) and Ba (202–968 ppm) contents, along with lower Rb/Sr (0.11–1.76) and higher Sr/Y (26.47–111.17) ratios (Figure 2). The tourmaline and garnet leucogranites both have TiO_2 (0.02–0.07 wt%), Sr (13–72 ppm), and Ba (6–187 ppm) contents systematically lower than the low Sr/Y two-mica leucogranite. Garnet leucogranites have the lowest $Mg^{\#}$ (14.84–27.63), Zr/Hf (11.15–19.31), and Eu/Eu* (0.10–0.29) among Himalayan leucogranites (Figure 2). The $Fe^{3+}/\Sigma Fe$ ratios of these leucogranite samples range from 0.00 to 0.55, with an average of 0.17 and a median of 0.15 (Figure 2f), similar to that of S-type granites (∼0.15) from the Lachlan Fold Belt (Chappell & White, 1992).

Sr-Nd isotope data of these Himalayan leucogranites show large variations (Table S5). The $^{87}Sr/^{86}Sr(i)$ and $\varepsilon_{Nd}(t)$ of low Sr/Y two-mica, tourmaline, and garnet leucogranites range from 0.7216 to 0.7674 and −16.0 to −12.4, respectively, showing affinity to the Himalayan metasedimentary rocks. However, the Sr-Nd isotopic composition of high Sr/Y leucogranite is relatively depleted ($^{87}Sr/^{86}Sr(i)$ = 0.7088–0.7175; $\varepsilon_{Nd}(t)$ = −11.1 to −10.2) and comparable to the metabasites in THS (Figure 3 and Table S5).

Nine kyanite-zone to sillimanite-zone schists and gneisses from Bhutan and Nepal show relatively homogenous δ^{56}Fe ranging from 0.05‰ to 0.15‰ with an average of 0.10 ± 0.08‰ (2SD), similar to values from global clastic sediments and the mean upper continental crust (δ^{56}Fe ∼0.10‰; Beard et al., 2003; Foden et al., 2015) (Table S6 and Figure 4). The tourmaline and two-mica leucogranites yield slightly isotopically heavier δ^{56}Fe, but with a limited range from 0.13‰ to 0.24‰ despite their large variations in petrology, elemental and Sr-Nd isotopic compositions (Figure 4). Garnet leucogranites have δ^{56}Fe (−0.04‰ to 0.06‰) lower than the other two types of leucogranites. Compared to the literature data, garnet leucogranites represent the lowest δ^{56}Fe end-member of granites at a given SiO_2.

Biotite (0.12‰–0.24‰) and tourmaline (ca. 0.15‰) have relatively consistent values among different samples, while muscovite has variable δ^{56}Fe sample by sample, ranging from 0.20‰ to 0.45‰. In YD1306 where biotite co-exists with tourmaline, $\delta^{56}Fe_{biotite}$ is marginally higher than $\delta^{56}Fe_{tourmaline}$, with a difference of 0.08 ± 0.04‰. Garnet has the lightest Fe isotopic composition with a δ^{56}Fe of −0.11‰ (Figure 5a). The similarity in δ^{56}Fe of the whole rock compared to biotite and tourmaline suggests that these minerals are the dominant Fe carrier in two-mica and tourmaline leucogranites respectively. This view is consistent with the observed mineral assemblages and EPMA analyses.

5. Discussion

5.1. Fe Isotopic Fractionation Factors Among Minerals and Melt

Iron isotope fractionation factors for a range of minerals and melt ($\Delta^{56}Fe_{mineral\text{-}melt}$) can be deduced from one certain mineral-melt fractionation and the inter-mineral fractionation using the equation

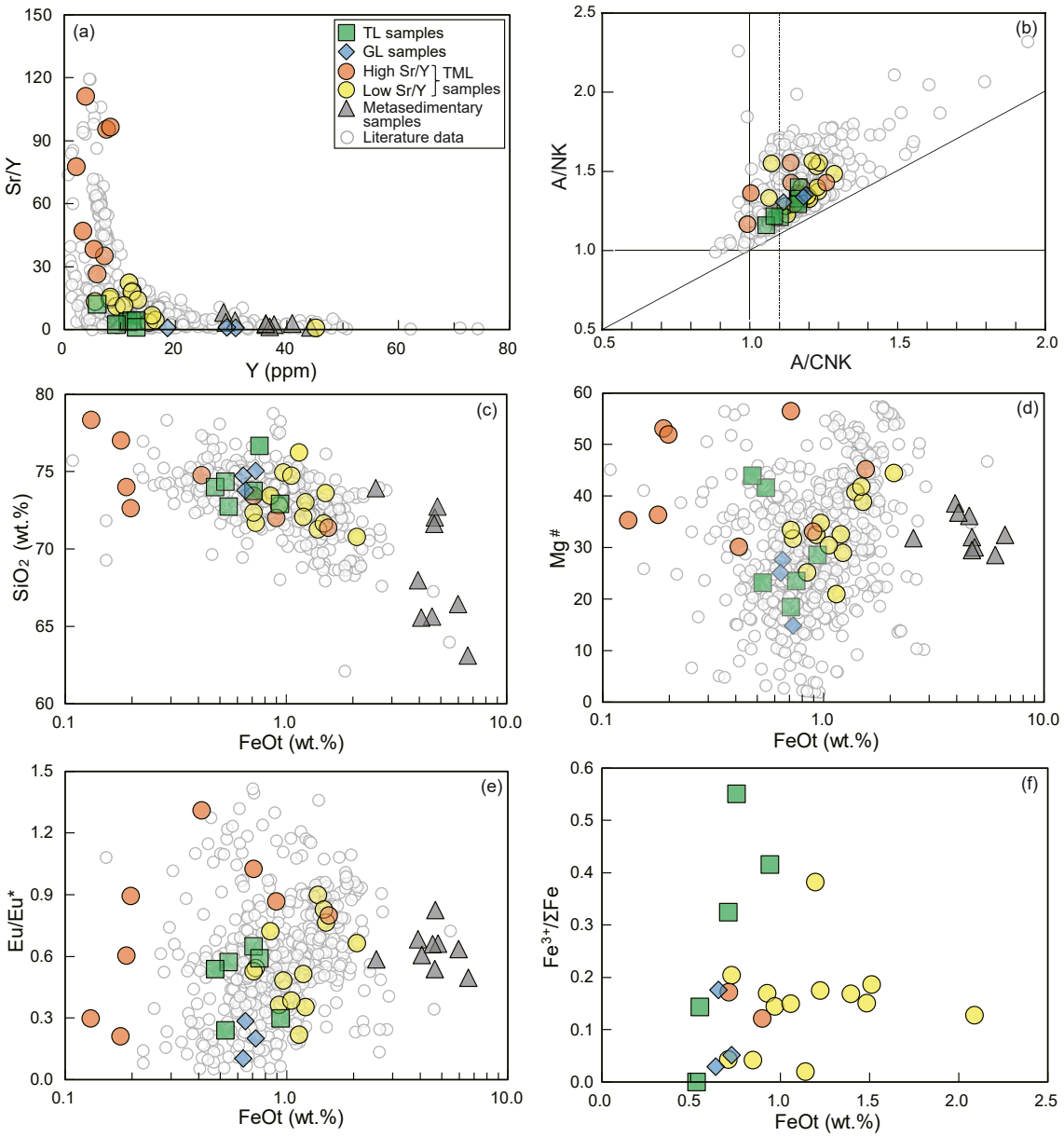

Figure 2. Diagrams of Sr/Y versus Y (a), A/NK versus A/CNK (b), SiO_2 versus FeOt (c), $Mg^{\#}$ versus FeOt (d), Eu/Eu* versus FeOt (e), and $Fe^{3+}/\Sigma Fe$ versus FeOt (f) for Himalayan leucogranites. A/NK = $Al_2O_3/(Na_2O + K_2O)$ in mole, A/CNK = $Al_2O_3/(CaO + Na_2O + K_2O)$ in mole. The literature data of Himalayan leucogranites are from: Aikman et al. (2012), Aoya et al. (2005), Carosi et al. (2013), Castelli and Lombardo (1988), L.-E. Gao et al. (2016a, 2017), L.-E. Gao and Zeng (2014), Gou et al. (2016), Guo and Wilson (2012), Harrison, Grove, Mckeegan, et al. (1999), Harrison and Wielicki (2016), Hopkinson (2016), Hou et al. (2012), G. Hu et al. (2017), Huang et al. (2017), Inger and Harris (1993), King et al. (2011), Lin et al. (2020), Z.-C. Liu et al. (2014, 2016), Scaillet et al. (1990), Searle et al. (1997), Shi et al. (2017), Visonà and Lombardo (2002), Z.-Z. Wang et al. (2020), Xie et al. (2019), Yang et al. (2019), Zeng et al. (2009), Zeng, Gao, Xie, and Liu-Zeng (2011), Zeng et al. (2015), Zeng et al. (2019), Zhang et al. (2004, 2005), and Zheng et al. (2016). Note that aplite, pegmatite, and hydrothermal altered samples are not shown. Abbreviations (also for the following figures) are: TL, tourmaline leucogranite; GL, garnet leucogranite; TML, two-mica leucogranite.

$\Delta^{56}Fe_{B\text{-}melt} = \Delta^{56}Fe_{A\text{-}melt} + \Delta^{56}Fe_{B\text{-}A}$ (A and B represent different minerals). $\Delta^{56}Fe_{biotite\text{-}melt}$ (~0.1‰) was calculated through the fractionation between the leucosomes and melanosomes of Black Hills migmatites where biotite is the dominant Fe carrier in the residua (Telus et al., 2012). This $\Delta^{56}Fe_{biotite\text{-}melt}$ can be influenced by the redox state of Fe in the melt and biotite, because phases with higher $Fe^{3+}/\Sigma Fe$ prefer heavier isotopes (Dauphas et al., 2014; Sossi & O'Neill, 2017). For a granitic melt, biotite tends to have similar $Fe^{3+}/\Sigma Fe$ to the melt under reductive conditions (Baker & Rutherford, 1996; Cesare et al., 2005). The Himalayan

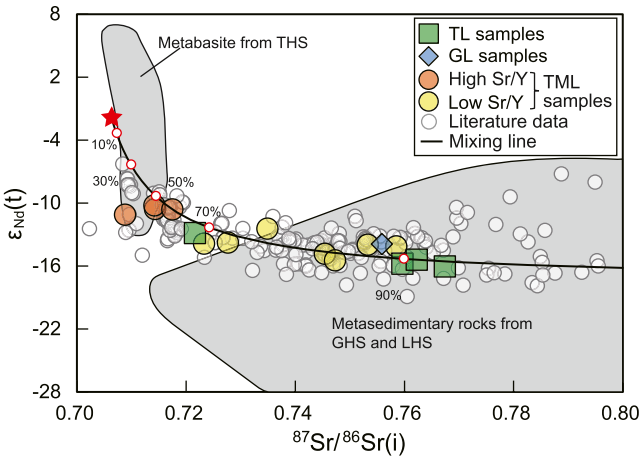

Figure 3. (a) Sr-Nd isotopic compositions of the investigated leucogranites. Himalayan leucogranites, metabasite from THS, and metasedimentary rocks previously reported from GHS and LHS are plotted for a comparison. Metasedimentary rocks in GHS and LHS and metabasite in THS are from Ahmad et al. (2000), Deniel et al. (1987), Inger and Harris (1993), Z.-C. Liu et al. (2014), Richards et al. (2005), Zeng et al. (2009), and Zeng, Gao, and Xie (2011). Literature data for leucogranites are from Deniel et al. (1987), L. Gao et al. (2015), L.-E. Gao et al. (2017), Gao and Zeng (2014), Guo and Wilson (2012), Harrison, Grove, Lovera, et al. (1999), Hou et al. (2012), G. Hu et al. (2017), Huang et al. (2017), Inger and Harris (1993), Ji et al. (2020), King et al. (2011), Lin et al. (2020), Z.-C. Liu et al. (2014), Zeng et al. (2009, 2019), Zeng, Gao, and Xie (2011); Zhang et al. (2004), and Zheng et al. (2016). The endmembers (high Sr/Y granite dike and Himalayan paragneiss) of mixing line are from Ji et al. (2020), whose compositions are listed in Table 1.

leucogranites have relatively low $Fe^{3+}/\Sigma Fe$ similar to the S-type granites in the Lachlan Fold Belt (Figure 2 and Chappell & White, 1992), and also to the Black Hills migmatites inferred to have formed under reducing conditions from the presence of graphite (Nabelek, 1999). Coordination of Fe in the melt tends to be reduced leading to a larger $\Delta^{56}Fe_{biotite\text{-}melt}$ with increasing SiO_2 and/or (Na + K)/(Ca + Mg) (Dauphas et al., 2014; Foden et al., 2015; He et al., 2017; Sossi et al., 2012). Himalayan leucogranites have comparable SiO_2 contents (70.80–78.36 wt%) and (Na + K)/(Ca + Mg) values (2.94–15.50) to the leucosomes of Black Hills migmatites (SiO_2: 72.46–79.45 wt%; (Na + K)/(Ca + Mg): 0.08–18.37; Nabelek, 1999). Accordingly, it is reasonable to apply the $\Delta^{56}Fe_{biotite\text{-}melt}$ estimated on a basis of Black Hills migmatites to the fractionation between biotite and Himalayan leucogranite melts.

The Fe isotopic fractionation factor between biotite and tourmaline has not been well-calibrated yet. Since Fe^{2+} occupies the octahedral site in both biotite and tourmaline (Hawthorne & Dirlam, 2011), they should have comparable Fe isotopic composition at the same $Fe^{3+}/\Sigma Fe$ ratio which is supported by the ab initio calculations (Nie et al., 2021). Tourmaline in the Himalayan leucogranite yields $\delta^{56}Fe$ slightly lower than biotite, with a $\Delta^{56}Fe_{biotite\text{-}tourmaline}$ of 0.08 ± 0.04‰. However, the $\Delta^{56}Fe_{biotite\text{-}tourmaline}$ constrained from Moosilauke metapelite is about −0.06 ± 0.03‰ at 700°C (Nie et al., 2021). This discrepancy may result from their different $Fe^{3+}/\Sigma Fe$ ratios and/or compositional variations in biotite and tourmaline (Nie et al., 2021; H. Wu et al., 2017).

Muscovite, like biotite, belongs to the mica group, and Fe in these minerals both occupies the same coordination sites (e.g., Fe^{2+} in the octahedral site), which suggests a $\Delta^{56}Fe_{biotite\text{-}muscovite}$ near 0 if these two minerals have a similar $Fe^{3+}/\Sigma Fe$. $\Delta^{56}Fe_{biotite\text{-}muscovite}$ in the Himalayan leucogranites, however, ranges from −0.31‰ to 0.04‰ (Figure 5). This indicates either isotope disequilibrium or mineral compositional control on isotope fractionation. Fe isotope equilibrium may have not been reached between muscovite and the other minerals, possibly due to the timing of their crystallization. For example, biotite crystallizes early near the liquidus while muscovite is a near-solidus phase (Scaillet et al., 1995). Thus some muscovite may occur within Fe-free domains of quartz and feldspar representing the last formed intergranular melt (Figure S2), hence impeding Fe isotope exchange with early crystallized biotite. Muscovite may record the variably heavy Fe isotopic compositions of the intergranular melts under near solidus conditions, which suggests that the $\delta^{56}Fe$ of melt could be significantly elevated after substantial crystallization of the leucogranites.

Given its euhedral shape with few inclusions, the garnet investigated here is magmatic (L.-E. Gao et al., 2012; Zeng et al., 2019), which is also consistent with its higher Mn contents (spessartine = 21%–29%, Grossular <1.92%; Table S7) than the xenocrystic garnets (spessartine < 5%; Harris et al., 1992) and lower Ca content than the peritectic garnet (Grossular = 11%–41%; King et al., 2011). Due to the lack of biotite in the garnet leucogranites, our data cannot provide direct constraints on the Fe isotopic fractionation between biotite and garnet. However, $\Delta^{56}Fe_{biotite\text{-}garnet}$ has been previously well calibrated by measurements of biotite-garnet pairs from metamorphosed iron formations, yielding a positive $\Delta^{56}Fe_{biotite\text{-}garnet} \sim 0.09\ (\pm 0.05) \times 10^6/T^2$ (Ye et al., 2020). This translates to a $\Delta^{56}Fe_{garnet\text{-}melt}$ ~−0.20‰ at 700°C, a crystallization temperature typical for Himalayan leucogranites.

Despite their low Fe contents, feldspars become important Fe carriers in high-Si granites. The Fe isotopic fractionation factors between biotite and feldspars have been calibrated from a suite of I-type granitoid in the Dabie orogen (H. Wu et al., 2017). The $\Delta^{56}Fe_{biotite\text{-}plagioclase}$ and $\Delta^{56}Fe_{biotite\text{-}alkali\text{-}feldspar}$ show linear relationships with the albite and orthoclase contents in plagioclase and alkali-feldspar, respectively ($\Delta^{56}Fe_{biotite\text{-}plagioclase} = 0.015 \times Ab\% - 0.48$; $\Delta^{56}Fe_{biotite\text{-}alkali\text{-}feldspar} = 0.026 \times Or\% - 1.35$), reflecting the compositional control on Fe isotope fractionation. From the typical compositions of plagioclase and K-feldspar in the Himalayan

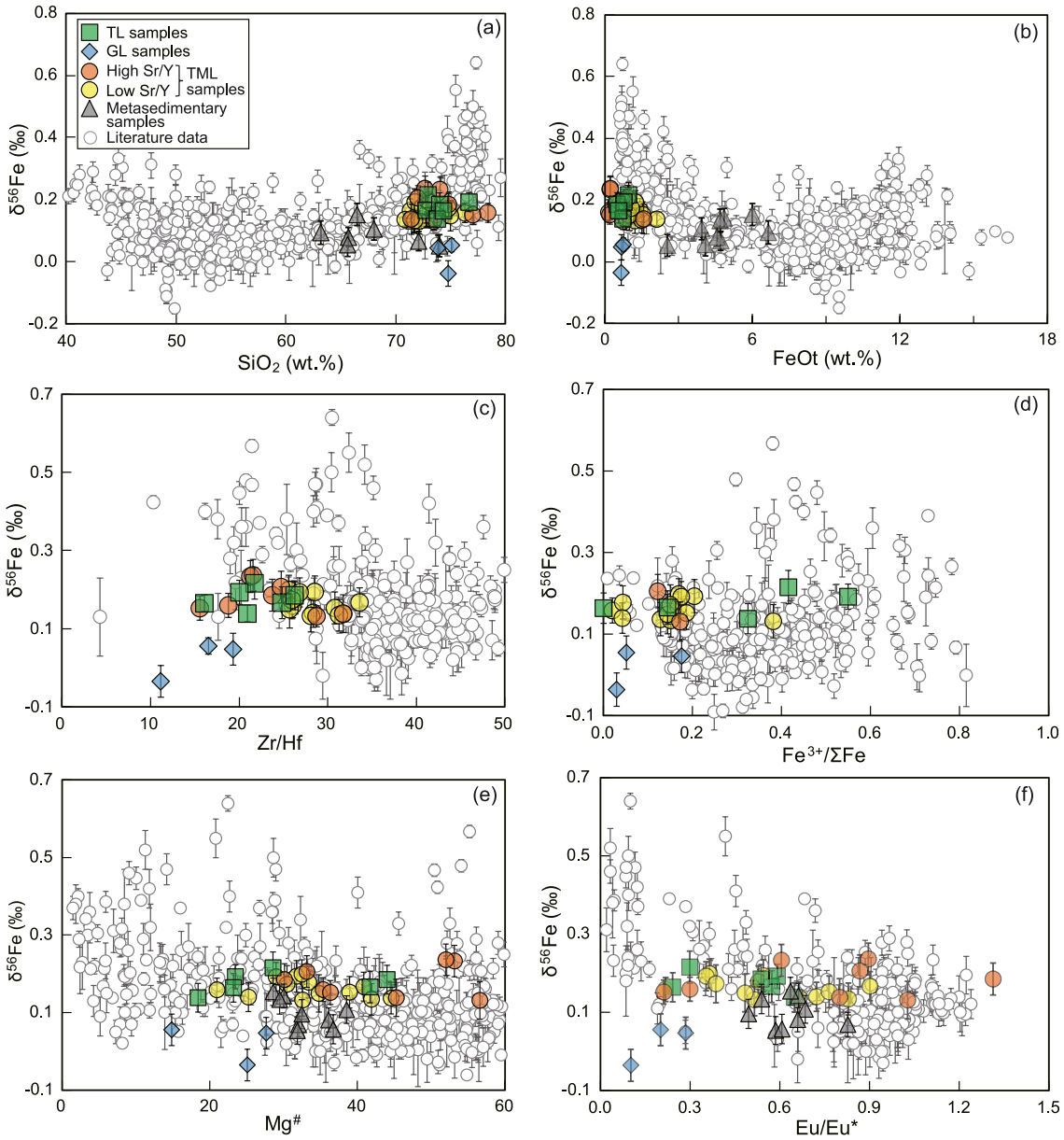

Figure 4. Diagrams of $\delta^{56}Fe$ versus SiO_2 (a), FeOt (b), Zr/Hf (c), $Fe^{3+}/\sum Fe$ (d), $Mg^{\#}$ (e), and Eu/Eu* (f). Global igneous rock data are from: Dauphas, Craddock, et al. (2009), Du et al. (2017), Foden et al. (2018), Foden et al. (2015), Gleeson et al. (2020), He et al. (2017, 2019), Heimann et al. (2008), Konter et al. (2016), Q.-W. Li et al. (2019), Poitrasson and Freydier. (2005), Schuessler et al. (2009), Sossi et al. (2012), Telus et al. (2012), Teng et al. (2008), Williams et al. (2018), H. Wu et al. (2017), Xia et al. (2017), and Zambardi et al. (2014).

leucogranites (Z.-C. Liu et al., 2019), the Ab% (in plagioclase) and Or% (in K-feldspar) were both assumed to be 90%, which indicates a $\Delta^{56}Fe_{biotite\text{-}plagioclase}$ of 0.77‰ and $\Delta^{56}Fe_{biotite\text{-}K\text{-}feldspar}$ of 0.89‰.

Accordingly, biotite, tourmaline, muscovite, and garnet are all predicted to be Fe isotopically lighter, while feldspars are isotopically heavier than the co-existing leucogranitic melt (summarized in Table 1).

5.2. Iron Isotope Fractionation of Himalayan Leucogranites

$\delta^{56}Fe$ of high-silica granites may be significantly elevated by the exclusion of isotopically light fluids, based on a negative correlation between $\delta^{56}Fe$ and Zr/Hf (Heimann et al., 2008; Poitrasson & Freydier, 2005). Note that melt Zr/Hf ratios may be also influenced by the dissolution/crystallization of zircon (Du et al., 2017;

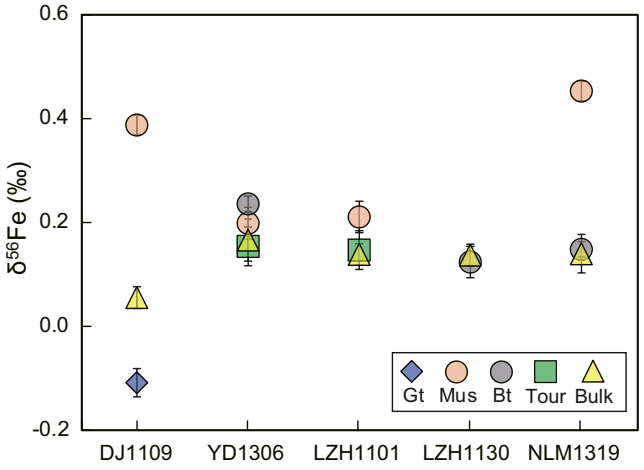

Figure 5. δ^{56}Fe of minerals separated from representative garnet, tourmaline, and two-mica leucogranites.

L.-E. Gao et al., 2017), and thus not be applied to tracing fluid exsolution for Himalayan leucogranites. Despite this, δ^{56}Fe does not increase with decreasing Zr/Hf from 33.59 to 11.15, nor is it correlated with either $TE_{1,3}$ (the degree of the lanthanide tetrad effect) or Y/Ho (Figures 4c and 6), which together argues against a significant role of fluid exsolution in fractionating melt δ^{56}Fe. The result here supports the previous conclusion that change in δ^{56}Fe during fluid exsolution may not be quantitatively important for high-silica granitic melts (Du et al., 2017). Our leucogranite samples were collected far away from the pluton boundary and without xenoliths, and are spread across both the Tethyan and High Himalayan leucogranite belts, greatly exceeding the length-scale that diffusion-driven isotope fractionation may influence natural samples (Teng et al., 2011; H. Wu et al., 2018; Zambardi et al., 2014) (Figure 1). Therefore, neither chemical nor thermal diffusion will be considered here.

It has been widely documented that the Himalayan leucogranites were generated by anatexis of metasedimentary rocks, except for the high Sr/Y two-mica leucogranites which are likely to have been derived from partial melting of metabasite (Harris & Massey, 1994; Le Fort, 1981; Patiño Douce & Harris, 1998; Zeng, Gao, & Xie, 2011; Zeng, Gao, Xie, & Liu-Zeng, 2011). Recently, it has been suggested that the Himalayan leucogranites represent highly fractionated granites, derived from a high degree of FC with or without assimilation (Ji et al., 2020; Z.-C. Liu et al., 2016, 2019; Z.-Z. Wang et al., 2020; F.-Y. Wu et al., 2020). In the following section, we will discuss the petrogenesis of Himalayan leucogranites based on a combination of Fe isotopic data with elemental and Sr-Nd isotope indices.

5.2.1. Fe Isotope Evidence and a Simple Fractional Crystallization Model

In an origin model requiring a high degree of FC for Himalayan leucogranites, there are two scenarios: (a) the two-mica leucogranites represent the cumulate rocks after extracting derivative liquids which crystallized as tourmaline and garnet leucogranites (F.-Y. Wu et al., 2020); (b) the two-mica, tourmaline and garnet leucogranites represent a magma differentiation series (Ji et al., 2020; C. Liu et al., 2020; Scaillet et al., 1990; Zeng et al., 2019). Given the lighter Fe isotopic compositions at any given index of differentiation, for example, SiO_2 and FeOt (Figure 4), garnet leucogranites, could not be controlled by the same mechanism as two-mica and tourmaline leucogranites and thus will be discussed separately.

Here we consider the possible effect of FC for two-mica and tourmaline leucogranites. For the Rayleigh fractionation model (Equation 1) and mass balance (Equation 2),

Table 1
The Partition Coefficients and Isotope Fractionation Factors for Minerals, and the Initial Melt and Country Rock Endmembers for AFC Modeling

	Biotite	Muscovite	Magnetite	Garnet	Tourmaline	Plagioclase	K-feldspar		Initial melt	Country rock
D_{Fe} in the literature	16.80–59.1[a,b]	5.17–6.01[a]	47.4–202[b]	48[c]	16–30[d]	0.028–0.099[e]	0.013–0.121[e]	Rb (ppm)	245	280
D_{Fe} used in this study	30	5.5	130	48	25	0.05	0.05	Sr (ppm)	844	40.2
D_{Rb}	3					0.05	0.3	FeOt (wt%)	2.86	6.81
D_{Sr}	0.05					6.5	6	$^{87}Sr/^{86}Sr(i)$	0.7064	0.8790
$\Delta^{56}Fe_{mineral\text{-}melt}$	−0.10	−0.10	0.20	−0.20	−0.18	0.77	0.89	δ^{56}Fe (‰)	0.14	0.10

Note. $\Delta^{56}Fe_{biotite\text{-}melt}$ was suggested to be 0.10‰ according to the fractionation in Black Hills migmatites where Fe in the melanosome is dominated by biotite (Telus et al., 2012). $\Delta^{56}Fe_{tourmaline\text{-}melt}$, $\Delta^{56}Fe_{garnet\text{-}melt}$, and $\Delta^{56}Fe_{magnetite\text{-}melt}$ were deduced based on the $\Delta^{56}Fe_{tourmaline\text{-}biotite}$ in Section 5.1 and the $\Delta^{56}Fe_{garnet\text{-}biotite}$ and $\Delta^{56}Fe_{magnetite\text{-}biotite}$ from Ye et al. (2020). $\Delta^{56}Fe_{muscovite\text{-}melt}$ was assumed to be the same as $\Delta^{56}Fe_{biotite\text{-}melt}$. $\Delta^{56}Fe_{plagioclase\text{-}melt}$ and $\Delta^{56}Fe_{K\text{-}feldspar\text{-}melt}$ were calculated by the relationship of $\Delta^{56}Fe_{plagioclase\text{-}biotite}$ and $\Delta^{56}Fe_{K\text{-}feldspar\text{-}biotite}$ assuming Ab% and Or% of plagioclase and K-feldspar is 90% (Z.-C. Liu et al., 2019; H. Wu et al., 2017). The geochemical composition of endmembers for AFC modeling was from Ji et al. (2020) and the Sr isotopic ratios were corrected at 20 Ma.

AFC, assimilation and fractional crystallization.

[a]Fe partition coefficients of these minerals in the literature were compiled from Icenhower and London (1995), [b]Ewart and Griffin (1994), [c]Sisson and Bacon (1992), [d]Benard et al. (1985), [e]H. Wu et al. (2017).

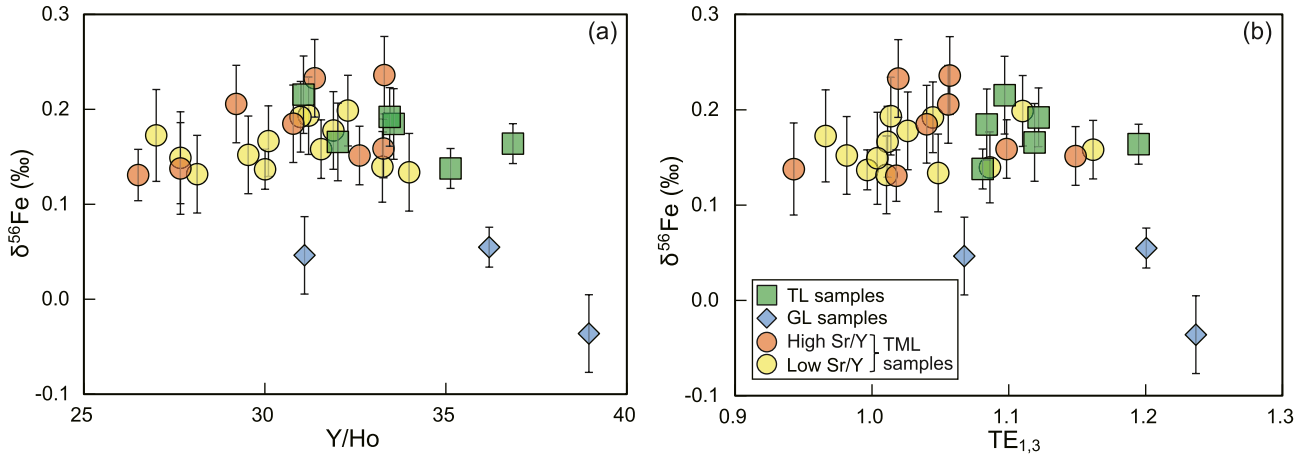

Figure 6. $\delta^{56}Fe$ variations with potential indices of fluid exsolution, for example, Y/Ho (a) and $TE_{1,3}$ (b). $TE_{1,3} = ((Ce_N \times Pr_N \times Tb \times Dy)/(La_N \times Nd_N \times Gd_N \times Ho_N))^{0.25}$ (Irber, 1999). The chondrite normalized data are from Boynton (1984).

$$\delta^{56}Fe_{melt} = \delta^{56}Fe_{melt0} + \Delta^{56}Fe_{crystal\text{-}melt} \times \ln(f_{Fe}), \quad (1)$$

$$\delta^{56}Fe_{melt0} = f_{Fe} \times \delta^{56}Fe_{melt} + (1 - f_{Fe}) \times \delta^{56}Fe_{average\ cumulate}, \quad (2)$$

we can obtain:

$$\Delta^{56}Fe_{crystal\text{-}melt} = \frac{(f_{Fe} - 1)}{\ln(f_{Fe})}\left(\delta^{56}Fe_{average\ cumulate} - \delta^{56}Fe_{melt}\right), \quad (3)$$

where f_{Fe} is the residual Fe fraction in the crystallizing melt and ranges from 1.0 to 0. For the first scenario, the isotopic difference ~0 between the average cumulate ($\delta^{56}Fe_{two\text{-}mica\ leucogranite} = 0.17 \pm 0.06‰$, 2SD) and residual melts ($\delta^{56}Fe_{tourmaline\ leucogranite} = 0.18 \pm 0.05‰$, 2SD) should be the maximum of $\Delta^{56}Fe_{crystal\text{-}melt}$ (note that $(f_{Fe} - 1) / \ln(f_{Fe})$ is always <1 and <<1 for an extreme degree of FC with $f_{Fe} \to 0$). However, this estimated $\Delta^{56}Fe_{crystal\text{-}melt}$ is inconsistent with the mineral assemblage (dominated by mica, feldspar, and quartz; Table S1) of the assumed cumulates (i.e., two-mica leucogranites), which yields a $\Delta^{56}Fe_{crystal\text{-}melt}$ between −0.05‰ and −0.10‰ (Figure 7b, see Table 1 for partition coefficients and fractionation factors which refer to discussions in Section 5.1). This scenario is therefore not appliable to the Himalayan leucogranites studied here. This view is also supported by the observation that some of the two-mica leucogranites show more evolved chemical compositions than the tourmaline leucogranites, for example, higher SiO_2 and lower FeOt.

If the two-mica and tourmaline leucogranites represent a cogenetic differentiation magma series, $\Delta^{56}Fe_{crystal\text{-}melt}$, required by a simple FC model to predict the whole rock $\delta^{56}Fe$, can be constrained by substituting $f_{Fe} = F_{melt} \times C_{melt}/C_{melt0}$ into the Rayleigh fractionation Equation 1, where F_{melt} is the mass fraction of residual melt. Given the difficulty of constraining F_{melt} for evolved granitic magmas, here we relate $\delta^{56}Fe_{melt}$ to C_{melt}/C_{melt0} through:

$$\frac{C_{melt}}{C_{melt0}} = F_{melt}^{(\bar{D}-1)}, \quad (4)$$

where $\bar{D}$ is the bulk partition coefficient of the crystallizing assemblage. Then we obtain:

$$\delta^{56}Fe_{melt} = \delta^{56}Fe_{melt0} + \Delta^{56}Fe_{crystal\text{-}melt} \times \frac{\bar{D}}{\bar{D} - 1} \times \ln\left(\frac{C_{melt}}{C_{melt0}}\right)\left(D \neq 1\right), \quad (5)$$

Note that in the case $\bar{D} = 1$, $\delta^{56}Fe_{melt}$ will change with no variation in C_{melt} (i.e., constant as C_{melt0}). A linear regression between $\delta^{56}Fe_{melt}$ and $\ln(C_{melt}/C_{melt0})$ indicates a slope (i.e., $\Delta^{56}Fe_{crystal\text{-}melt} \times (\bar{D} / \bar{D} - 1)$) of −0.02 (Figure 7a). As FeOt of two-mica and tourmaline leucogranites decreases with increasing SiO_2, $\bar{D}$ should

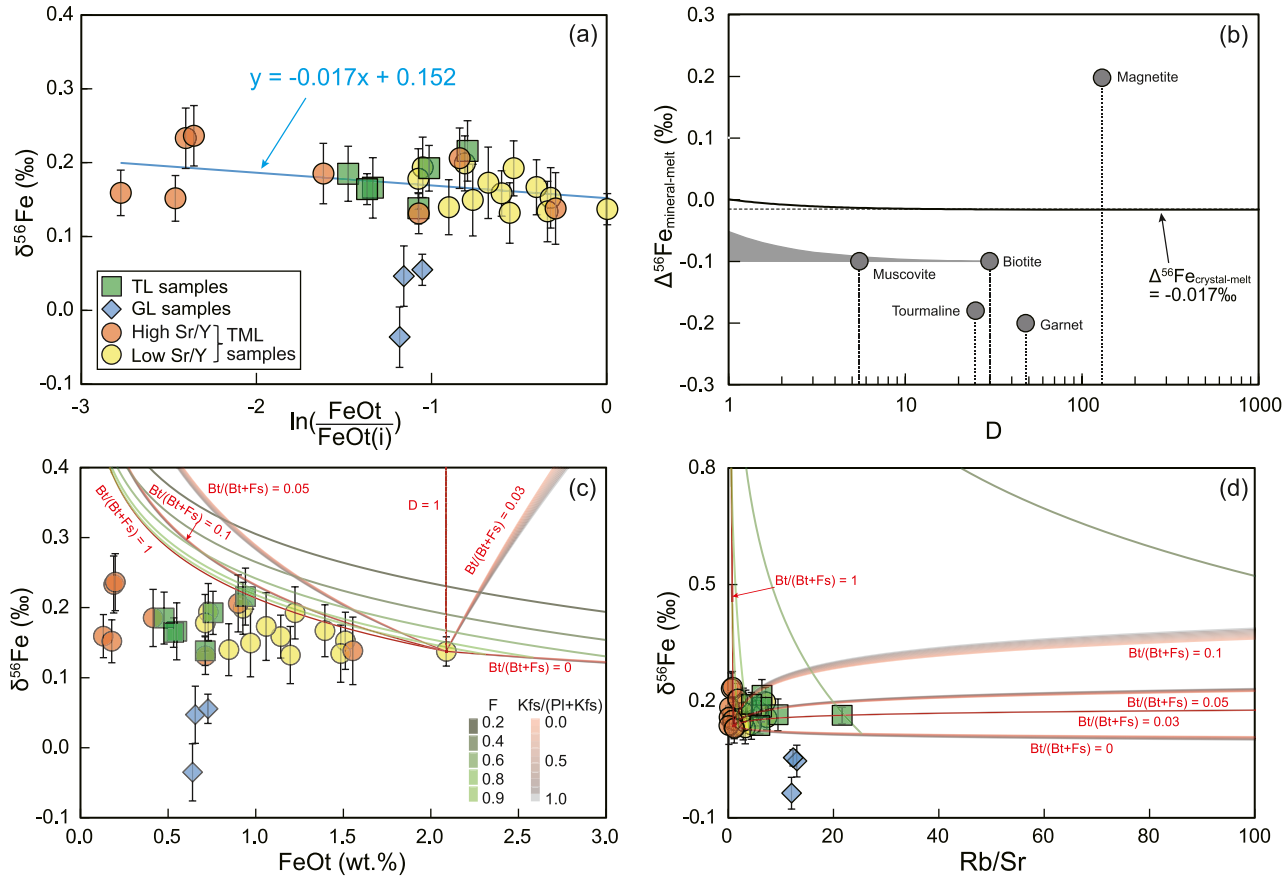

Figure 7. (a) A linear fit between the δ^{56}Fe and ln(FeOt/FeOt(i)) for two-mica and tourmaline leucogranites. (b) Diagram of estimated $\Delta^{56}Fe_{mineral\text{-}melt}$ versus $D(Fe)_{mineral\text{-}melt}$. The possible Fe isotope fractionation factor between a crystallizing assemblage of quartz + plagioclase + K-feldspar + muscovite + biotite and the melt is given as the gray field. Isotopic effect of fractional crystallization is illustrated along with changes in FeOt and Rb/Sr in (c) and (d), respectively. Green-gray contour lines contour the evolved compositions with given F_{melt}.

be higher than unity, which suggests a $\Delta^{56}Fe_{crystal\text{-}melt}$ between 0‰ and −0.02‰ (Figure 7b). Again, this estimate cannot be easily explained by the mineral assemblages observed in our samples (see discussions above).

It is possible that the crystallizing assemblage during magma differentiation differed from the assemblage observed in the granites. Hereafter we further test the possibility of a high degree of FC considering varying crystallizing mineral assemblages. Potential major liquidus phases include plagioclase, K-feldspar, quartz, biotite, muscovite, tourmaline, and garnet (Huang et al., 2017; Inger & Harris, 1993; Z.-C. Liu et al., 2019; Scaillet et al., 1990, 1995; Z.-Z. Wang et al., 2020). Quartz is free of Fe and thus not considered here. Biotite is considered as the only Fe-rich mineral to provide the minimum estimate of potential isotope fractionation, for the reasons below: (a) the fractionation factors of other Fe-rich minerals (i.e., muscovite, tourmaline, and garnet) are either similar to or greater than $\Delta^{56}Fe_{biotite\text{-}melt}$ (Sossi & O'Neill, 2017; Ye et al., 2020 and this study); and (b) magnetite which is isotopically heavier (Heimann et al., 2008; Sossi & O'Neill, 2017; Telus et al., 2012; H. Wu et al., 2017; Ye et al., 2020), is absent based on petrological observations and experimental results (Scaillet et al., 1995; F.-Y. Wu et al., 2020). Magnetite has neither been observed in thin sections of our samples nor has been separated by magnet from whole-rock powders. Moreover, significant crystallization of magnetite will result in a decrease in Fe/Mn along with δ^{56}Fe (Sossi et al., 2012), which is inconsistent with the observation (Figure 9b). FC from an initial melt represented by sample LZH1130 with the maximum FeOt in this study is illustrated in Figures 7c and 7d, given a crystallizing assemblage of biotite, plagioclase, and K-feldspar with variable proportions and parameters listed in Table 1. Rb/Sr of the differentiating melt is dominantly controlled by mica and feldspars and thus also considered here (Harris &

Inger, 1992). The calculated curves lead to two striking inferences: (a) the evolved melt tends to have δ^{56}Fe higher than Himalayan leucogranite at a given FeOt, especially when F_{melt} is low; (b) the limited δ^{56}Fe variation of Himalayan leucogranite indicates a $\Delta^{56}Fe_{crystal\text{-}melt} \sim 0$, which implies a crystallizing assemblage of a low biotite/(biotite + feldspars) mode ratio. Extreme crystallization of such an assemblage would produce high Rb/Sr ratios that have not been observed. Overall, an extreme degree of FC, on its own can be ruled out as the origin of tourmaline and two-mica leucogranites.

5.2.2. Assimilation and Fractional Crystallization Model

Simultaneous assimilation of metasedimentary rocks with δ^{56}Fe around 0.10‰ may have counteracted Fe isotope fractionation caused by FC. An assimilation and fractional crystallization (AFC) model has been previously proposed to explain the large variation of Sr-Nd isotopic ratios of Himalayan leucogranites (Ji et al., 2020). Ji et al. (2020) considered high Sr/Y samples with depleted Sr-Nd isotope compositions as the primary melt that was generated by partial melting of amphibolite, and suggested that the other leucogranites can be produced by an AFC process. Fe isotopic systematics during AFC has been illustrated in Figure 8 (DePaolo, 1981). As discussed in Section 5.2.1, a biotite + felspars crystallizing assemblage is adopted with partitioning and fractionation parameters from Table 1. δ^{56}Fe of the initial melt and the country rock are assumed to be 0.14‰ and 0.10‰, typical of I-type granites (Foden et al., 2015) and Himalayan metasedimentary rocks (this study) respectively. Rb and Sr contents, as well as Sr isotopic systematics, are also considered, and elemental contents and $^{87}Sr/^{86}Sr(i)$ of end-members are from Ji et al. (2020). Given the high FeOt of local country rocks (e.g., 6.81 wt% in Ji et al., 2020 and 4.68 ± 1.18 wt% of metasedimentary rocks here), a higher r (i.e., the ratio of assimilation rate to fractional crystallization rate) requires more biotite in the crystallizing assemblage to cause a decrease in FeOt, which means a larger value for $\Delta^{56}Fe_{crystal\text{-}melt}$ and a higher δ^{56}Fe of the evolved melt (Figure 8). The δ^{56}Fe-FeOt trend of Himalayan leucogranites can only be reproduced by AFC when r and F_{melt} are both low, for example, $r = 0.2$ and $F_{melt} < 0.4$. In this case, the calculated melt should have an Rb/Sr substantially higher than the assumed initial melt and country rock (e.g., >100) and $^{87}Sr/^{86}Sr(i)$ close to that of the country rock, which, however, are not consistent with observations on Himalayan leucogranites. Accordingly, a high degree of FC with simultaneous assimilation is also unable to account for the origin of tourmaline and two-mica leucogranites.

5.2.3. The Role of Crustal Anatexis

Although some degree of FC cannot be completely ruled out in the origin of Himalayan tourmaline and two-mica leucogranites, as discussed above, an extreme degree of FC is not supported by the Fe isotopic data presented in this study. δ^{56}Fe and chemical compositions of these granites are unlikely to have been significantly affected after extraction from their sources. The highly variable elemental and Sr-Nd-Hf-O isotopic compositions of Himalayan leucogranites thus can be attributed to source heterogeneity and diverse melting reactions (Guillot & Le Fort, 1995; Inger & Harris, 1993; Knesel & Davidson, 2002; Le Fort, 1975; Patiño Douce & Harris, 1998; Zeng, Gao, & Xie, 2011). The supposed sources may range from metabasites for high Sr/Y leucogranites with relatively depleted Sr-Nd isotopic compositions (Figure 3; Hou et al., 2012; Zeng, Gao, Xie, & Liu-Zeng, 2011) to metasedimentary rocks for low Sr/Y two-mica and tourmaline leucogranites with relatively enriched Sr-Nd isotopic compositions (L.-E. Gao et al., 2017; Harrison, Grove, Mckeegan, et al., 1999; Inger & Harris, 1993; Le Fort et al., 1987). Since metabasite and metasediments both have δ^{56}Fe ~ 0.10‰ (e.g., Teng et al., 2013 and this study), δ^{56}Fe of two-mica and tourmaline leucogranites are higher than their supposed sources by 0.07 ± 0.06 ‰ (2SD, $N = 27$). This value is consistent with isotope fractionation that was observed in migmatites from Black Hill and the Dabie orogen, that is, $\Delta^{56}Fe_{leucosome\text{-}melanosome}$ from 0.04‰ to 0.20‰ (Telus et al., 2012; L.-J. Xu et al., 2017), and most likely reflects isotope fractionation during crustal anatexis.

5.2.4. Origin of Low δ^{56}Fe Garnet Leucogranites

Given all major Fe-rich minerals in the magmatic system, for example, biotite, muscovite, tourmaline, and garnet have $\Delta^{56}Fe_{crystal\text{-}melt} < 0$, the low δ^{56}Fe of garnet leucogranites cannot be explained by isotope fractionation during either FC or crustal anatexis. Garnet in this type of leucogranite show euhedral shape and few inclusions with higher Mn and lower Ca contents (spessartine = 21%–29%, Grossular <1.92%; Table S7) than examples of xenocrystic garnet (spessartine < 5%; Harris et al., 1992) or peritectic garnet (Grossular = 11%–41%; King et al., 2011), thus indicating a probable magmatic origin (L.-E. Gao et al., 2012;

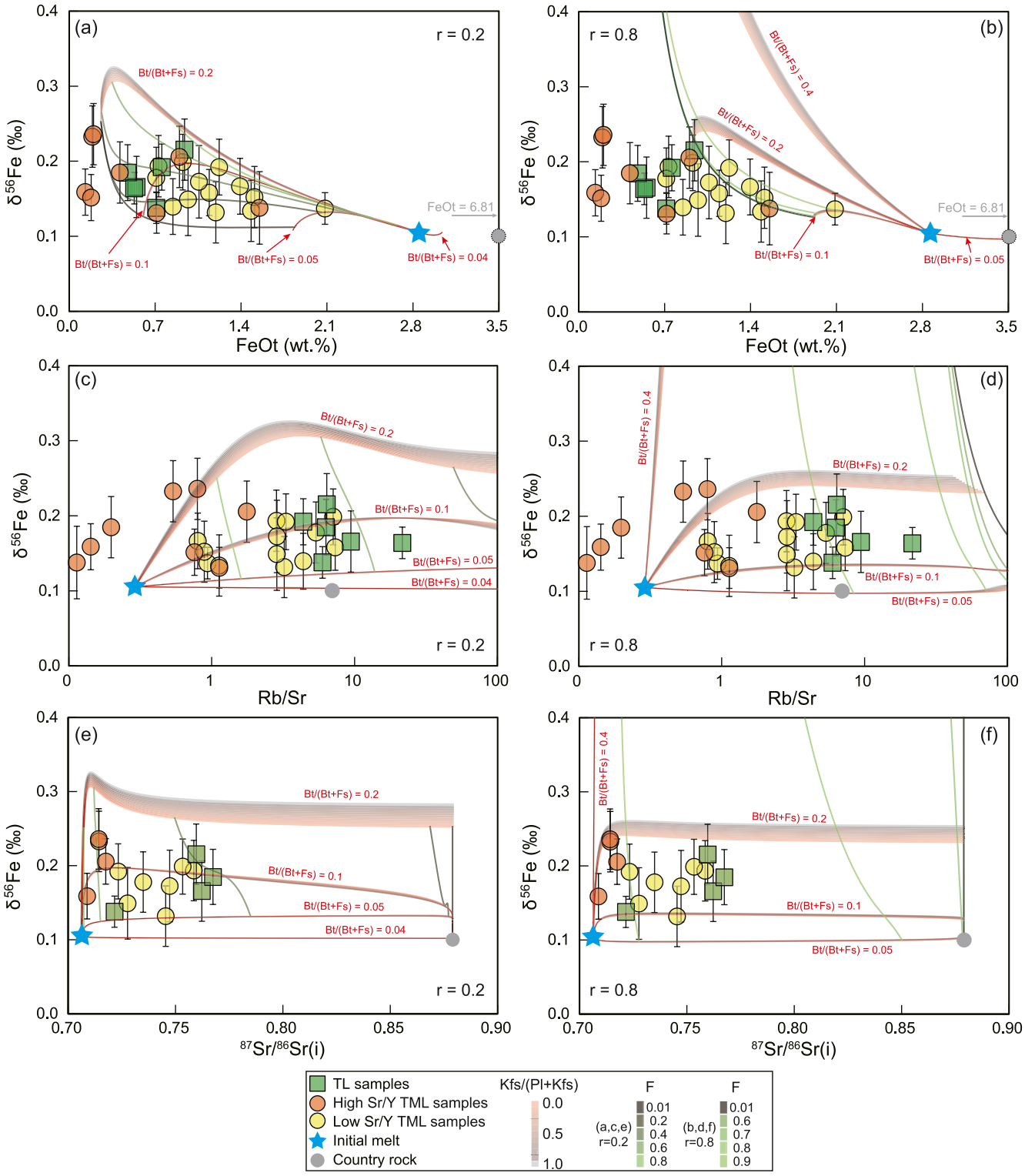

Figure 8. Illustration of an AFC process with $r = 0.2$ and 0.8. The details of primitive melt and country rock were listed in Table 1 and discussed in the text. Same as in Figure 7, Green-gray contour lines contour the evolved compositions with given F_{melt}.

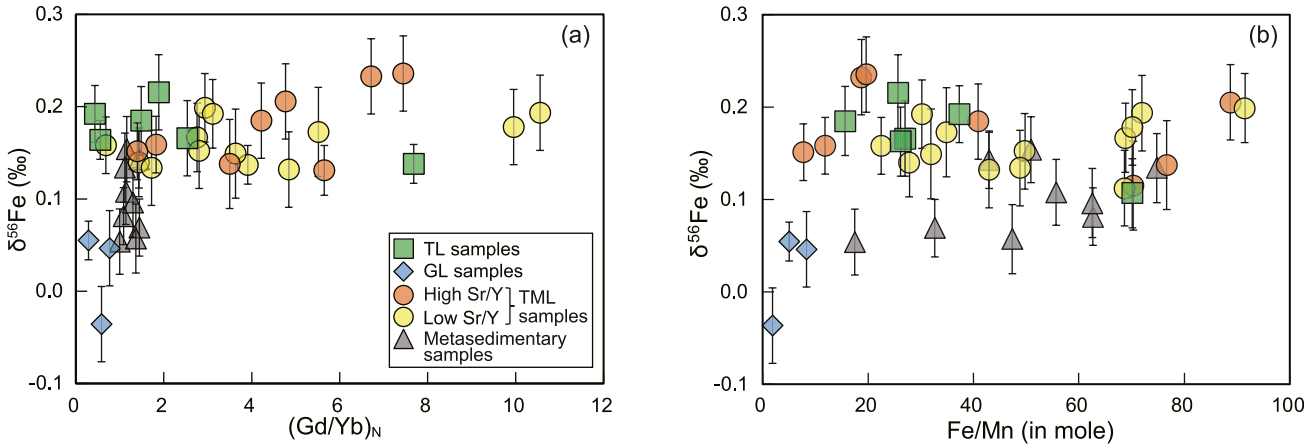

Figure 9. $\delta^{56}Fe$ versus $(Gd/Yb)_N$ (a) and $\delta^{56}Fe$ versus Fe/Mn (in mole) (b) diagrams where the garnet leucogranites have the relatively lower $\delta^{56}Fe$, $(Gd/Yb)_N$, and Fe/Mn values.

Zeng et al., 2019). Accumulation of this mineral in garnet leucogranites is indicated by their low $(Gd/Yb)_N$ (0.29–0.77), Fe/Mn (1.80–8.26, in mole) (Figure 9), and HREE contents higher than the other leucogranites (Figure S1). The low $\delta^{56}Fe$ of garnet leucogranites thus can be explained by accumulation of magmatic garnet that hosts the lightest iron isotopes of the rock-forming minerals (Figures 5a and 7b). A simple binary mixing calculation suggests that the addition of only 2.2 wt% garnets in equilibrium with a low FeOt melt, represented by sample DL1703, can model the $\delta^{56}Fe$ of garnet leucogranites down to −0.04‰, which is consistent with the garnet content estimation by microscope observation. Nevertheless, the mechanism for garnet crystallization remains largely unknown, possibly due to the special pristine melt composition of garnet leucogranites.

6. Conclusion

To elucidate the role of partial melting and FC in generating Himalayan leucogranites, we report Fe isotope data of 30 Himalayan leucogranites and 9 metasedimentary rocks, supplemented with mineral-pair measurement as well as geochemical and Sr-Nd isotopes data. Local metasedimentary rocks yield $\delta^{56}Fe \sim 0.10‰$, typical of global clastic sediments. Garnet leucogranites are isotopically lighter with $\delta^{56}Fe$ ranging from −0.04‰ to 0.06‰, possibly due to garnet accumulation. The tourmaline and two-mica leucogranites show roughly homogeneous $\delta^{56}Fe$ from 0.13‰ to 0.24‰ without resolvable change with variable SiO_2 (70.80–78.36 wt%), MgO (0.04–0.94 wt%), FeOt (0.13–2.09 wt%), $Mg^{\#}$ (18.41–56.53), and Eu*/Eu (0.21–1.31). FC and AFC modeling suggest that they could not have experienced a high degree of FC. The higher $\delta^{56}Fe$ relative to the supposed sources (by ~0.07‰), probably reflects isotope fractionation during crustal anatexis. This study therefore confirms that the geochemical and isotopic characteristics of Himalayan leucogranite can be used to reflect the P - T - X_{H_2O} conditions of partial melting, as indicators of the thermal and tectonic evolution of Himalayan crust and orogen.

Data Availability Statement

The supporting information involved in this study is available from the Figshare Repository (https://doi.org/10.6084/m9.figshare.14828346).

Acknowledgments
Constructive reviews from R. Mathur and the other anonymous reviewer, and the efficient handling from Professor Mark Dekkers and John Lassiter are greatly appreciated. This study is supported by the Second Tibetan Plateau Scientific Expedition and Research (STEP) program (Grant no. 2019QZKK0702), the National Natural Science Foundation of China (Grant no. 41688103), the National Key Research and Development Project of China (Project 2016YFC0600304), the 111 Project of the Ministry of Science and Technology, China (Grant no. BP0719021) and the fellowship from the China Scholarship Council. Bhutan samples were collected by Tom Hopkinson and Stacy Phillips, supported by NERC studentship grants (NE/K501074/1, NEE2152S BUFI). This is CUGB petrogeochemical contribution No. PGC-201574.

References

Ahmad, T., Harris, N., Bickle, M., Chapman, H., Bunbury, J., & Prince, C. (2000). Isotopic constraints on the structural relationships between the lesser Himalayan series and the high Himalayan crystalline series, Garhwal Himalaya. *The Geological Society of America Bulletin*, *112*, 467–477. https://doi.org/10.1130/0016-7606(2000)112<467:ICOTSR>2.0

Aikman, A. B., Harrison, T. M., & Hermann, J. (2012). The origin of Eo- and Neo-Himalayan granitoids, Eastern Tibet. *Journal of Asian Earth Sciences*, *58*, 143–157. https://doi.org/10.1016/j.jseaes.2012.05.018

Aikman, A. B., Harrison, T. M., & Lin, D. (2008). Evidence for early (>44 Ma) Himalayan crustal thickening, Tethyan Himalaya, southeastern Tibet. *Earth and Planetary Science Letters*, *274*(1–2), 14–23. https://doi.org/10.1016/j.epsl.2008.06.038

Aoya, M., Wallis, S. R., Terada, K., Lee, J., Kawakami, T., Wang, Y., & Heizler, M. (2005). North-south extension in the Tibetan crust triggered by granite emplacement. *Geology*, *33*(11), 853–856. https://doi.org/10.1130/G21806.1

Baker, L. L., & Rutherford, M. J. (1996). The effect of dissolved water on the oxidation state of silicic melts. *Geochimica et Cosmochimica Acta*, *60*(12), 2179–2187. https://doi.org/10.1016/0016-7037(96)00090-7

Beard, B. L., Johnson, C. M., Von Damm, K. L., & Poulson, R. L. (2003). Iron isotope constraints on Fe cycling and mass balance in oxygenated Earth oceans. *Geology*, *31*(7), 629–632. https://doi.org/10.1130/0091-7613(2003)031<0629:iicofc>2.0.co;2

Benard, F., Moutou, P., & Pichavant, M. (1985). Phase relations of tourmaline leucogranites and the significance of tourmaline in silicic magmas. *The Journal of Geology*, *93*(3), 271–291. https://doi.org/10.1086/628952

Boynton, W. V. (1984). Cosmochemistry of the rare Earth elements: Meteorite studies. In P. Henderson (Ed.), *Rare Earth element geochemistry* (pp. 63–114). Elsevier. https://doi.org/10.1016/b978-0-444-42148-7.50008-3

Carosi, R., Montomoli, C., & Iaccarino, S. (2018). 20 years of geological mapping of the metamorphic core across Central and Eastern Himalayas. *Earth-Science Reviews*, *177*, 124–138. https://doi.org/10.1016/j.earscirev.2017.11.006

Carosi, R., Montomoli, C., Rubatto, D., & Visona, D. (2013). Leucogranite intruding the South Tibetan Detachment in western Nepal: Implications for exhumation models in the Himalayas. *Terra Nova*, *25*(6), 478–489. https://doi.org/10.1111/ter.12062

Castelli, D., & Lombardo, B. (1988). The Gophu La and western Lunana granites: Miocene muscovite leucogranites of the Bhutan Himalaya. *Lithos*, *21*(3), 211–225. https://doi.org/10.1016/0024-4937(88)90010-2

Cesare, B., Meli, S., Nodari, L., & Russo, U. (2005). Fe^{3+} reduction during biotite melting in graphitic metapelites: Another origin of CO_2 in granulites. *Contributions to Mineralogy and Petrology*, *149*(2), 129–140. https://doi.org/10.1007/s00410-004-0646-3

Chappell, B. W., & White, A. J. R. (1992). I- and S-type granites in the Lachlan Fold Belt. *Transactions of the Royal Society of Edinburgh Earth Sciences*, *83*(1–2), 1–26. https://doi.org/10.1017/s0263593300007720

Craddock, P. R., & Dauphas, N. (2011). Iron isotopic compositions of geological reference materials and chondrites. *Geostandards and Geoanalytical Research*, *35*(1), 101–123. https://doi.org/10.1111/j.1751-908X.2010.00085.x

Dauphas, N., Craddock, P. R., Asimow, P. D., Bennett, V. C., Nutman, A. P., & Ohnenstetter, D. (2009). Iron isotopes may reveal the redox conditions of mantle melting from Archean to Present. *Earth and Planetary Science Letters*, *288*(1–2), 255–267. https://doi.org/10.1016/j.epsl.2009.09.029

Dauphas, N., Pourmand, A., & Teng, F.-Z. (2009). Routine isotopic analysis of iron by HR-MC-ICPMS: How precise and how accurate? *Chemical Geology*, *267*(3), 175–184. https://doi.org/10.1016/j.chemgeo.2008.12.011

Dauphas, N., Roskosz, M., Alp, E. E., Neuville, D. R., Hu, M. Y., Sio, C. K., et al. (2014). Magma redox and structural controls on iron isotope variations in Earth's mantle and crust. *Earth and Planetary Science Letters*, *398*, 127–140. https://doi.org/10.1016/j.epsl.2014.04.033

Deniel, C., Vidal, P., Fernandez, A., Le Fort, P., & Peucat, J.-J. (1987). Isotopic study of the Manaslu granite (Himalaya, Nepal): Inferences on the age and source of Himalayan leucogranites. *Contributions to Mineralogy and Petrology*, *96*(1), 78–92. https://doi.org/10.1007/BF00375529

DePaolo, D. J. (1981). Trace element and isotopic effects of combined wallrock assimilation and fractional crystallization. *Earth and Planetary Science Letters*, *53*(2), 189–202. https://doi.org/10.1016/0012-821X(81)90153-9

Ding, L., Kapp, P., & Wan, X. (2005). Paleocene-Eocene record of ophiolite obduction and initial India-Asia collision, south central Tibet. *Tectonics*, *24*(3), TC3001. https://doi.org/10.1029/2004tc001729

Du, D.-H., Wang, X.-L., Yang, T., Chen, X., Li, J.-Y., & Li, W. (2017). Origin of heavy Fe isotope compositions in high-silica igneous rocks: A rhyolite perspective. *Geochimica et Cosmochimica Acta*, *218*, 58–72. https://doi.org/10.1016/j.gca.2017.09.014

Ewart, A., & Griffin, W. L. (1994). Application of proton-microprobe data to trace-element partitioning in volcanic rocks. *Chemical Geology*, *117*(1), 251–284. https://doi.org/10.1016/0009-2541(94)90131-7

Fan, J.-J., Wang, Q., Li, J., Wei, G.-J., Ma, J.-L., Ma, L., et al. (2021). Boron and molybdenum isotopic fractionation during crustal anatexis: Constraints from the Conadong leucogranites in the Himalayan Block, South Tibet. *Geochimica et Cosmochimica Acta*, *297*, 120–142. https://doi.org/10.1016/j.gca.2021.01.005

Foden, J., Sossi, P. A., & Nebel, O. (2018). Controls on the iron isotopic composition of global arc magmas. *Earth and Planetary Science Letters*, *494*, 190–201. https://doi.org/10.1016/j.epsl.2018.04.039

Foden, J., Sossi, P. A., & Wawryk, C. M. (2015). Fe isotopes and the contrasting petrogenesis of A-, I- and S-type granite. *Lithos*, *212–215*, 32–44. https://doi.org/10.1016/j.lithos.2014.10.015

France-Lanord, C., Sheppard, S. M. F., & Lefort, P. (1988). Hydrogen and oxygen isotope variations in the High Himalaya peraluminous Manaslu leucogranite. *Geochimica et Cosmochimica Acta*, *52*(2), 513–526. https://doi.org/10.1016/0016-7037(88)90107-x

Gao, L., Zeng, L. S., Xu, Z. Q., & Wang, L. (2015). Himalaya in the Caledonia time: A record from the Malashan-Gyirong area, southern Tibet. *Acta Petrologica Sinica*, *31*(5), 1200–1218.

Gao, L.-E., Zeng, L., & Asimow, P. D. (2017). Contrasting geochemical signatures of fluid-absent versus fluid-fluxed melting of muscovite in metasedimentary sources: The Himalayan leucogranites. *Geology*, *45*(1), 39–42. https://doi.org/10.1130/g38336.1

Gao, L.-E., Zeng, L., Gao, J., Shang, Z., Hou, K., & Wang, Q. (2016). Oligocene crustal anatexis in the Tethyan Himalaya, southern Tibet. *Lithos*, *264*, 201–209. https://doi.org/10.1016/j.lithos.2016.08.038

Gao, L.-E., Zeng, L., Shi, W., Chen, Z., Hu, G., & Sun, D. (2012). Two types of garnets in the Cenozoic granites from the Himalayan Orogenic Belt: Geohemical characteristics and implications for crustal anatexis. *Acta Petrologica Sinica*, *28*(9), 2963–2980.

Gao, L. E., & Zeng, L. S. (2014). Fluxed melting of metapelite and the formation of Miocene high-CaO two-mica granites in the Malashan gneiss dome, southern Tibet. *Geochimica et Cosmochimica Acta*, *130*, 136–155. https://doi.org/10.1016/j.gca.2014.01.003

Gao, P., Zheng, Y.-F., & Zhao, Z.-F. (2016). Distinction between S-type and peraluminous I-type granites: Zircon versus whole-rock geochemistry. *Lithos*, *258–259*, 77–91. https://doi.org/10.1016/j.lithos.2016.04.019

Gleeson, M. L. M., Gibson, S. A., & Williams, H. M. (2020). Novel insights from Fe-isotopes into the lithological heterogeneity of Ocean Island Basalts and plume-influenced MORBs. *Earth and Planetary Science Letters*, *535*, 116114. https://doi.org/10.1016/j.epsl.2020.116114

Gou, Z., Zhang, Z., Dong, X., Xiang, H., Ding, H., Tian, Z., & Lei, H. (2016). Petrogenesis and tectonic implications of the Yadong leucogranites, southern Himalaya. *Lithos*, *256–257*, 300–310. https://doi.org/10.1016/j.lithos.2016.04.009

Guillot, S., & Le Fort, P. (1995). Geochemical constraints on the bimodal origin of high Himalayan leucogranites. *Lithos*, *35*(3), 221–234. https://doi.org/10.1016/0024-4937(94)00052-4

Guo, Z., & Wilson, M. (2012). The Himalayan leucogranites: Constraints on the nature of their crustal source region and geodynamic setting. *Gondwana Research*, *22*(2), 360–376. https://doi.org/10.1016/j.gr.2011.07.027

Harris, N., & Massey, J. (1994). Decompression and anatexis of Himalayan metapelites. *Tectonics*, *13*(6), 1537–1546. https://doi.org/10.1029/94TC01611

Harris, N. B. W., Gravestock, P., & Inger, S. (1992). Ion-microprobe determinations of trace-element concentrations in garnets from anatectic assemblages. *Chemical Geology*, *100*(1), 41–49. https://doi.org/10.1016/0009-2541(92)90101-A

Harris, N. B. W., & Inger, S. (1992). Trace element modelling of pelite-derived granites. *Contributions to Mineralogy and Petrology*, *110*(1), 46–56. https://doi.org/10.1007/bf00310881

Harrison, T. M., Grove, M., Lovera, O. M., Catlos, E. J., & D'Andrea, J. (1999). The origin of Himalayan anatexis and inverted metamorphism: Models and constraints. *Journal of Asian Earth Sciences*, *17*(5–6), 755–772. https://doi.org/10.1016/S1367-9120(99)00018-8

Harrison, T. M., Grove, M., Mckeegan, K. D., Coath, C. D., Lovera, O. M., & Fort, P. L. (1999). Origin and episodic emplacement of the Manaslu Intrusive Complex, Central Himalaya. *Journal of Petrology*, *40*(1), 3–19. https://doi.org/10.1093/petroj/40.1.3

Harrison, T. M., & Wielicki, M. M. (2016). From the Hadean to the Himalaya: 4.4 Ga of felsic terrestrial magmatism. *American Mineralogist*, *101*(6), 1348–1359. https://doi.org/10.2138/am-2016-5516

Hawthorne, F. C., & Dirlam, D. M. (2011). Tourmaline the indicator mineral: From atomic arrangement to Viking navigation. *Elements*, *7*(5), 307–312. https://doi.org/10.2113/gselements.7.5.307

He, Y., Ke, S., Teng, F.-Z., Wang, T., Wu, H., Lu, Y., & Li, S. (2015). High-precision iron isotope analysis of geological reference materials by high-resolution MC-ICP-MS. *Geostandards and Geoanalytical Research*, *39*(3), 341–356. https://doi.org/10.1111/j.1751-908X.2014.00304.x

He, Y., Meng, X., Ke, S., Wu, H., Zhu, C., Teng, F.-Z., et al. (2019). A nephelinitic component with unusual δ^{56}Fe in Cenozoic basalts from eastern China and its implications for deep oxygen cycle. *Earth and Planetary Science Letters*, *512*, 175–183. https://doi.org/10.1016/j.epsl.2019.02.009

He, Y., Wu, H., Ke, S., Liu, S.-A., & Wang, Q. (2017). Iron isotopic compositions of adakitic and non-adakitic granitic magmas: Magma compositional control and subtle residual garnet effect. *Geochimica et Cosmochimica Acta*, *203*, 89–102. https://doi.org/10.1016/j.gca.2017.01.005

Heimann, A., Beard, B. L., & Johnson, C. M. (2008). The role of volatile exsolution and sub-solidus fluid/rock interactions in producing high ^{56}Fe/^{54}Fe ratios in siliceous igneous rocks. *Geochimica et Cosmochimica Acta*, *72*(17), 4379–4396. https://doi.org/10.1016/j.gca.2008.06.009

Hodges, K. V. (2000). Tectonics of the Himalaya and southern Tibet from two perspectives. *The Geological Society of America Bulletin*, *112*(3), 324–350. https://doi.org/10.1130/0016-7606(2000)112<324:tothas>2.0.co;2

Hopkinson, T. (2016). *Geochemical insights into crustal melting in the Bhutan Himalaya (Doctoral disseration)*. The Open University.

Hopkinson, T. N., Harris, N. B. W., Roberts, N. M. W., Warren, C. J., Hammond, S., Spencer, C. J., & Parrish, R. R. (2019). Evolution of the melt source during protracted crustal anatexis: An example from the Bhutan Himalaya. *Geology*, *48*, 87–91. https://doi.org/10.1130/g47078.1

Hopkinson, T. N., Harris, N. B. W., Warren, C. J., Spencer, C. J., Roberts, N. M. W., Horstwood, M. S. A., et al. (2017). The identification and significance of pure sediment-derived granites. *Earth and Planetary Science Letters*, *467*, 57–63. https://doi.org/10.1016/j.epsl.2017.03.018

Hou, Z.-Q., Zheng, Y.-C., Zeng, L.-S., Gao, L.-E., Huang, K.-X., Li, W., et al. (2012). Eocene-Oligocene granitoids in southern Tibet: Constraints on crustal anatexis and tectonic evolution of the Himalayan orogen. *Earth and Planetary Science Letters*, *349–350*, 38–52. https://doi.org/10.1016/j.epsl.2012.06.030

Hu, G., Zeng, L., Gao, L., Chen, H., Liu, Q., & Gao, Y. (2017). Anatexis of Paleoproterozoic rock units in the Gurla Mandhata dome, Himalayan orogen. *Acta Petrologica Sinica*, *33*(12), 3710–3728.

Hu, X., Garzanti, E., Wang, J., Huang, W., An, W., & Webb, A. (2016). The timing of India-Asia collision onset—Facts, theories, controversies. *Earth-Science Reviews*, *160*, 264–299. https://doi.org/10.1016/j.earscirev.2016.07.014

Huang, C., Zhao, Z., Li, G., Zhu, D.-C., Liu, D., & Shi, Q. (2017). Leucogranites in Lhozag, southern Tibet: Implications for the tectonic evolution of the eastern Himalaya. *Lithos*, *294–295*, 246–262. https://doi.org/10.1016/j.lithos.2017.09.014

Icenhower, J., & London, D. (1995). An experimental study of element partitioning among biotite, muscovite, and coexisting peraluminous silicic melt at 200 MPa (H_2O). *American Mineralogist*, *80*(11–12), 1229–1251. https://doi.org/10.2138/am-1995-11-1213

Inger, S., & Harris, N. (1993). Geochemical constraints on leucogranite magmatism in the Langtang Valley, Nepal Himalaya. *Journal of Petrology*, *34*(2), 345–368. https://doi.org/10.1093/petrology/34.2.345

Irber, W. (1999). The lanthanide tetrad effect and its correlation with K/Rb, Eu/Eu*, Sr/Eu, Y/Ho, and Zr/Hf of evolving peraluminous granite suites. *Geochimica et Cosmochimica Acta*, *63*(3–4), 489–508. https://doi.org/10.1016/s0016-7037(99)00027-7

Ji, W.-Q., Wu, F.-Y., Liu, X.-C., Liu, Z.-C., Zhang, C., Liu, T., et al. (2020). Pervasive Miocene melting of thickened crust from the Lhasa terrane to Himalaya, southern Tibet and its constraint on generation of Himalayan leucogranite. *Geochimica et Cosmochimica Acta*, *278*, 137–156. https://doi.org/10.1016/j.gca.2019.07.048

King, J., Harris, N., Argles, T., Parrish, R., & Zhang, H. (2011). Contribution of crustal anatexis to the tectonic evolution of Indian crust beneath southern Tibet. *The Geological Society of America Bulletin*, *123*(1–2), 218–239. https://doi.org/10.1130/b30085.1

Knesel, K. M., & Davidson, J. P. (2002). Insights into collisional magmatism from isotopic fingerprints of melting reactions. *Science*, *296*(5576), 2206–2208. https://doi.org/10.1126/science.1070622

Kohn, M. J. (2014). Himalayan metamorphism and its tectonic implications. *Annual Review of Earth and Planetary Sciences*, *42*(1), 381–419. https://doi.org/10.1146/annurev-earth-060313-055005

Konter, J. G., Pietruszka, A. J., Hanan, B. B., Finlayson, V. A., Craddock, P. R., Jackson, M. G., & Dauphas, N. (2016). Unusual δ^{56}Fe values in Samoan rejuvenated lavas generated in the mantle. *Earth and Planetary Science Letters*, *450*, 221–232. https://doi.org/10.1016/j.epsl.2016.06.029

Le Fort, P. (1975). Himalayas: The collided range. Present knowledge of the continental arc. *American Journal of Science*, *275*(1), 1–44.

Le Fort, P. (1981). Manaslu leucogranite: A collision signature of the Himalaya: A model for its genesis and emplacement. *Journal of Geophysical Research*, *86*(B11), 10545–10568. https://doi.org/10.1029/JB086iB11p10545

Le Fort, P., Cuney, M., Deniel, C., Francelanord, C., Sheppard, S. M. F., Upreti, B. N., & Vidal, P. (1987). Crustal generation of the Himalayan leucogranites. *Tectonophysics*, *134*(1–3), 39–57. https://doi.org/10.1016/0040-1951(87)90248-4

Li, C.-F., Chen, F., & Li, X.-H. (2007). Precise isotopic measurements of sub-nanogram Nd of standard reference material by thermal ionization mass spectrometry using the NdO^+ technique. *International Journal of Mass Spectrometry*, *266*(1–3), 34–41. https://doi.org/10.1016/j.ijms.2007.06.013

Li, Q.-W., Nebel, O., Nebel-Jacobsen, Y., Richter, M., Wang, R., Weinberg, R., et al. (2019). Crustal reworking at convergent margins traced by Fe isotopes in I-type intrusions from the Gangdese arc, Tibetan Plateau. *Chemical Geology*, *510*, 47–55. https://doi.org/10.1016/j.chemgeo.2019.02.007

Lin, C., Zhang, J., Wang, X., Putthapiban, P., Zhang, B., & Huang, T. (2020). Oligocene initiation of the South Tibetan Detachment System: Constraints from syn-tectonic leucogranites in the Kampa Dome, Northern Himalaya. *Lithos*, *354–355*, 105332. https://doi.org/10.1016/j.lithos.2019.105332

Liu, C., Wang, R.-C., Wu, F.-Y., Xie, L., Liu, X.-C., Li, X.-K., et al. (2020). Spodumene pegmatites from the Pusila pluton in the higher Himalaya, South Tibet: Lithium mineralization in a highly fractionated leucogranite batholith. *Lithos*, *358–359*, 358–359. https://doi.org/10.1016/j.lithos.2020.105421

Liu, D., Zhao, Z., DePaolo, D. J., Zhu, D.-C., Meng, F.-Y., Shi, Q., & Wang, Q. (2017). Potassic volcanic rocks and adakitic intrusions in southern Tibet: Insights into mantle-crust interaction and mass transfer from Indian plate. *Lithos*, *268–271*, 48–64. https://doi.org/10.1016/j.lithos.2016.10.034

Liu, X.-C., Li, X.-H., Liu, Y., Yang, L., Li, Q.-L., Wu, F.-Y., et al. (2018). Insights into the origin of purely sediment-derived Himalayan leucogranites: Si-O isotopic constraints. *Science Bulletin*, *63*, 1243–1245. https://doi.org/10.1016/j.scib.2018.09.001

Liu, Y., Zong, K., Kelemen, P. B., & Gao, S. (2008). Geochemistry and magmatic history of eclogites and ultramafic rocks from the Chinese continental scientific drill hole: Subduction and ultrahigh-pressure metamorphism of lower crustal cumulates. *Chemical Geology*, *247*(1–2), 133–153. https://doi.org/10.1016/j.chemgeo.2007.10.016

Liu, Z.-C., Wu, F.-Y., Ding, L., Liu, X.-C., Wang, J.-G., & Ji, W.-Q. (2016). Highly fractionated late Eocene (35 Ma) leucogranite in the Xiaru Dome, Tethyan Himalaya, South Tibet. *Lithos*, *240–243*, 337–354. https://doi.org/10.1016/j.lithos.2015.11.026

Liu, Z.-C., Wu, F.-Y., Ji, W.-Q., Wang, J.-G., & Liu, C.-Z. (2014). Petrogenesis of the Ramba leucogranite in the Tethyan Himalaya and constraints on the channel flow model. *Lithos*, *208–209*, 118–136. https://doi.org/10.1016/j.lithos.2014.08.022

Liu, Z.-C., Wu, F.-Y., Liu, X.-C., Wang, J.-G., Yin, R., Qiu, Z.-L., et al. (2019). Mineralogical evidence for fractionation processes in the Himalayan leucogranites of the Ramba Dome, southern Tibet. *Lithos*, *340–341*, 71–86. https://doi.org/10.1016/j.lithos.2019.05.004

Ma, Q., Zheng, J., Griffin, W. L., Zhang, M., Tang, H., Su, Y., & Ping, X. (2012). Triassic "adakitic" rocks in an extensional setting (North China): Melts from the cratonic lower crust. *Lithos*, *149*, 159–173. https://doi.org/10.1016/j.lithos.2012.04.017

Markl, G., von Blanckenburg, F., & Wagner, T. (2006). Iron isotope fractionation during hydrothermal ore deposition and alteration. *Geochimica et Cosmochimica Acta*, *70*(12), 3011–3030. https://doi.org/10.1016/j.gca.2006.02.028

Nabelek, P. I. (1999). Trace element distribution among rock-forming minerals in Black Hills migmatites, South Dakota; A case for solid-state equilibrium. *American Mineralogist*, *84*(9), 1256–1269. https://doi.org/10.2138/am-1999-0904

Nie, N. X., Dauphas, N., Alp, E. E., Zeng, H., Sio, C. K., Hu, J. Y., et al. (2021). Iron, magnesium, and titanium isotopic fractionations between garnet, ilmenite, fayalite, biotite, and tourmaline: Results from NRIXS, ab initio, and study of mineral separates from the Moosilauke metapelite. *Geochimica et Cosmochimica Acta*, *302*, 18–45. http://10.1016/j.gca.2021.03.014

Patiño Douce, A. E., & Harris, N. (1998). Experimental constraints on Himalayan anatexis. *Journal of Petrology*, *39*(4), 689–710. https://doi.org/10.1093/petroj/39.4.689

Poitrasson, F., & Freydier, R. (2005). Heavy iron isotope composition of granites determined by high resolution MC-ICP-MS. *Chemical Geology*, *222*(1–2), 132–147. https://doi.org/10.1016/j.chemgeo.2005.07.005

Richards, A., Argles, T., Harris, N., Parrish, R., Ahmad, T., Darbyshire, F., & Draganits, E. (2005). Himalayan architecture constrained by isotopic tracers from clastic sediments. *Earth and Planetary Science Letters*, *236*(3–4), 773–796. https://doi.org/10.1016/j.epsl.2005.05.034

Scaillet, B., France-Lanord, C., & Le Fort, P. (1990). Badrinath-Gangotri plutons (Garhwal, India): Petrological and geochemical evidence for fractionation processes in a high Himalayan leucogranite. *Journal of Volcanology and Geothermal Research*, *44*(1), 163–188. https://doi.org/10.1016/0377-0273(90)90017-A

Scaillet, B., Pichavant, M., & Roux, J. (1995). Experimental crystallization of leucogranite magmas. *Journal of Petrology*, *36*(3), 663–705. https://doi.org/10.1093/petrology/36.3.663

Schuessler, J. A., Schoenberg, R., & Sigmarsson, O. (2009). Iron and lithium isotope systematics of the Hekla volcano, Iceland—Evidence for Fe isotope fractionation during magma differentiation. *Chemical Geology*, *258*(1–2), 78–91. https://doi.org/10.1016/j.chemgeo.2008.06.021

Searle, M. P., Parrish, R. R., Hodges, K. V., Hurford, A., Ayres, M. W., & Whitehouse, M. J. (1997). Shisha Pangma leucogranite, south Tibetan Himalaya: Field relations, geochemistry, age, origin, and emplacement. *The Journal of Geology*, *105*(3), 295–318. https://doi.org/10.1086/515924

Shi, Q., Huang, C., Lei, H., Qi, N., Tong, X., & Zhao, Z. (2017). Geochronology, geochemistry, and petrogenesis of Yamarong leucogranite in Tsona area. *Acta Petrologica Sinica*, *33*(8), 2454–2466.

Sisson, T. W., & Bacon, C. R. (1992). Garnet/high-silica rhyolite trace element partition coefficients measured by ion microprobe. *Geochimica et Cosmochimica Acta*, *56*(5), 2133–2136. https://doi.org/10.1016/0016-7037(92)90336-H

Sossi, P. A., Foden, J. D., & Halverson, G. P. (2012). Redox-controlled iron isotope fractionation during magmatic differentiation: An example from the Red Hill intrusion, S. Tasmania. *Contributions to Mineralogy and Petrology*, *164*(5), 757–772. https://doi.org/10.1007/s00410-012-0769-x

Sossi, P. A., & O'Neill, H. S. C. (2017). The effect of bonding environment on iron isotope fractionation between minerals at high temperature. *Geochimica et Cosmochimica Acta*, *196*, 121–143. https://doi.org/10.1016/j.gca.2016.09.017

Telus, M., Dauphas, N., Moynier, F., Tissot, F. L. H., Teng, F.-Z., Nabelek, P. I., et al. (2012). Iron, zinc, magnesium and uranium isotopic fractionation during continental crust differentiation: The tale from migmatites, granitoids, and pegmatites. *Geochimica et Cosmochimica Acta*, *97*, 247–265. https://doi.org/10.1016/j.gca.2012.08.024

Teng, F.-Z., Dauphas, N., & Helz, R. T. (2008). Iron isotope fractionation during magmatic differentiation in Kilauea Iki Lava Lake. *Science*, *320*(5883), 1620–1622. https://doi.org/10.1126/science.1157166

Teng, F.-Z., Dauphas, N., Helz, R. T., Gao, S., & Huang, S. (2011). Diffusion-driven magnesium and iron isotope fractionation in Hawaiian olivine. *Earth and Planetary Science Letters*, *308*(3–4), 317–324. https://doi.org/10.1016/j.epsl.2011.06.003

Teng, F.-Z., Dauphas, N., Huang, S., & Marty, B. (2013). Iron isotopic systematics of oceanic basalts. *Geochimica et Cosmochimica Acta*, *107*, 12–26. https://doi.org/10.1016/j.gca.2012.12.027

Visonà, D., & Lombardo, B. (2002). Two-mica and tourmaline leucogranites from the Everest-Makalu region (Nepal-Tibet). Himalayan leucogranite genesis by isobaric heating? *Lithos*, *62*(3–4), 125–150. https://doi.org/10.1016/S0024-4937(02)00112-3

Wang, R., Wu, F., Xie, L., Liu, X., Wang, J., Yang, L., et al. (2017). A preliminary study of rare-metal mineralization in the Himalayan leucogranite belts, South Tibet. *Science China Earth Sciences*, *60*(9), 1655–1663. https://doi.org/10.1007/s11430-017-9075-8

Wang, Y., Zhu, X.-k., Mao, J.-w., Li, Z.-h., & Cheng, Y.-b. (2011). Iron isotope fractionation during skarn-type metallogeny: A case study of Xinqiao Cu-S-Fe-Au deposit in the Middle-Lower Yangtze valley. *Ore Geology Reviews*, *43*(1), 194–202. https://doi.org/10.1016/j.oregeorev.2010.12.004

Wang, Z.-Z., Liu, S.-A., Liu, Z.-C., Zheng, Y.-C., & Wu, F.-Y. (2020). Extreme Mg and Zn isotope fractionation recorded in the Himalayan leucogranites. *Geochimica et Cosmochimica Acta*, *278*, 305–321. https://doi.org/10.1016/j.gca.2019.09.026
Weinberg, R. F. (2016). Himalayan leucogranites and migmatites: Nature, timing and duration of anatexis. *Journal of Metamorphic Geology*, *34*(8), 821–843. https://doi.org/10.1111/jmg.12204
Williams, H. M., Prytulak, J., Woodhead, J. D., Kelley, K. A., Brounce, M., & Plank, T. (2018). Interplay of crystal fractionation, sulfide saturation and oxygen fugacity on the iron isotope composition of arc lavas: An example from the Marianas. *Geochimica et Cosmochimica Acta*, *226*, 224–243. https://doi.org/10.1016/j.gca.2018.02.008
Wu, F., Liu, X., Ji, W., Wang, J., & Yang, L. (2017). Highly fractionated granites: Recognition and research. *Science China Earth Sciences*, *60*, 11219. https://doi.org/10.1007/s11430-016-5139-1
Wu, F., Liu, Z., Liu, X., & Ji, W. (2015). Himalayan leucogranite: Petrogenesis and implications to orogenesis and plateau uplift. *Acta Petrologica Sinica*, *31*(1), 1–36.
Wu, F.-Y., Liu, X.-C., Liu, Z.-C., Wang, R.-C., Xie, L., Wang, J.-M., et al. (2020). Highly fractionated Himalayan leucogranites and associated rare-metal mineralization. *Lithos*, *352–353*, 105319. https://doi.org/10.1016/j.lithos.2019.105319
Wu, H., He, Y., Bao, L., Zhu, C., & Li, S. (2017). Mineral composition control on inter-mineral iron isotopic fractionation in granitoids. *Geochimica et Cosmochimica Acta*, *198*, 208–217. https://doi.org/10.1016/j.gca.2016.11.008
Wu, H., He, Y., Teng, F.-Z., Ke, S., Hou, Z., & Li, S. (2018). Diffusion-driven magnesium and iron isotope fractionation at a gabbro-granite boundary. *Geochimica et Cosmochimica Acta*, *222*, 671–684. https://doi.org/10.1016/j.gca.2017.11.010
Xia, Y., Li, S., & Huang, F. (2017). Iron and Zinc isotope fractionation during magmatism in the continental crust: Evidence from bimodal volcanic rocks from Hailar basin, NE China. *Geochimica et Cosmochimica Acta*, *213*, 35–46. https://doi.org/10.1016/j.gca.2017.06.018
Xie, L., Tao, X., Wang, R., Wu, F., Liu, C., Liu, X., et al. (2019). Highly fractionated leucogranites in the eastern Himalayan Cuonadong dome and related magmatic Be-Nb-Ta and hydrothermal Be-W-Sn mineralization. *Lithos*, *354–355*, 105286. https://doi.org/10.1016/j.lithos.2019.105286
Xu, L.-J., He, Y., Wang, S.-J., Wu, H., & Li, S. (2017). Iron isotope fractionation during crustal anatexis: Constraints from migmatites from the Dabie orogen, Central China. *Lithos*, *284–285*, 171–179. https://doi.org/10.1016/j.lithos.2017.04.005
Xu, Z., Wang, Q., Pecher, A., Liang, F., Qi, X., Cai, Z., et al. (2013). Orogen-parallel ductile extension and extrusion of the Greater Himalaya in the late Oligocene and Miocene. *Tectonics*, *32*(2), 191–215. https://doi.org/10.1002/tect.20021
Yang, L., Liu, X.-C., Wang, J.-M., & Wu, F.-Y. (2019). Is Himalayan leucogranite a product by in situ partial melting of the Greater Himalayan Crystalline? A comparative study of leucosome and leucogranite from Nyalam, southern Tibet. *Lithos*, *342–343*, 542–556. https://doi.org/10.1016/j.lithos.2019.06.007
Ye, H., Wu, C., Brzozowski, M. J., Yang, T., Zha, X., Zhao, S., et al. (2020). Calibrating equilibrium Fe isotope fractionation factors between magnetite, garnet, amphibole, and biotite. *Geochimica et Cosmochimica Acta*, *271*, 78–95. https://doi.org/10.1016/j.gca.2019.12.014
Yin, A. (2006). Cenozoic tectonic evolution of the Himalayan orogen as constrained by along-strike variation of structural geometry, exhumation history, and foreland sedimentation. *Earth-Science Reviews*, *76*(1–2), 1–131. https://doi.org/10.1016/j.earscirev.2005.05.004
Yin, A., & Harrison, T. M. (2000). Geologic evolution of the Himalayan-Tibetan orogen. *Annual Review of Earth and Planetary Sciences*, *28*(28), 211–280. https://doi.org/10.1146/annurev.earth.28.1.211
Zambardi, T., Lundstrom, C. C., Li, X., & McCurry, M. (2014). Fe and Si isotope variations at Cedar Butte volcano: Insight into magmatic differentiation. *Earth and Planetary Science Letters*, *405*, 169–179. https://doi.org/10.1016/j.epsl.2014.08.020
Zeng, L., Gao, L.-E., Tang, S., Hou, K., Guo, C., & Hu, G. (2015). Eocene magmatism in the Tethyan Himalaya, southern Tibet. *Geological Society, London, Special Publications*, *412*(1), 287–316. https://doi.org/10.1144/sp412.8
Zeng, L., Gao, L. E., & Xie, K. (2011). Concurrence of Mid-Miocene high Sr/Y granite and leucogranite in the Yardoi gneiss dome, Tethyan Himalaya, Southern Tibet. *Mineralogical Magazine*, *75*(3), 2245.
Zeng, L., Gao, L.-E., Xie, K., & Liu-Zeng, J. (2011). Mid-Eocene high Sr/Y granites in the Northern Himalayan Gneiss Domes: Melting thickened lower continental crust. *Earth and Planetary Science Letters*, *303*(3–4), 251–266. https://doi.org/10.1016/j.epsl.2011.01.005
Zeng, L., Liu, J., Gao, L., Xie, K., & Wen, L. (2009). Early Oligocene anatexis in the Yardoi gneiss dome, southern Tibet and geological implications. *Chinese Science Bulletin*, *54*(1), 104–112. https://doi.org/10.1007/s11434-008-0362-x
Zeng, L., Zhao, L., Gao, L.-E., Hou, K., & Wang, Q. (2019). Magmatic garnet from Mid-Miocene cogenetic high Sr/Y granite and leucogranite from the Himalayan orogenic belt, southern Tibet. *Acta Petrologica Sinica*, *35*(6), 1599–1626.
Zhang, H., Harris, N., Parrish, R., Kelley, S., Zhang, L., Rogers, N., et al. (2004). Causes and consequences of protracted melting of the mid-crust exposed in the North Himalayan antiform. *Earth and Planetary Science Letters*, *228*(1–2), 195–212. https://doi.org/10.1016/j.epsl.2004.09.031
Zhang, H., Harris, N., Parrish, R., Zhang, L., Zhao, Z., & Li, D. (2005). Geochemistry of North Himalayan leucogranites: Regional comparison, petrogenesis and tectonic implications. *Earth Science*, *30*(3), 275–288.
Zheng, Y.-c., Hou, Z.-q., Fu, Q., Zhu, D.-C., Liang, W., & Xu, P. (2016). Mantle inputs to Himalayan anatexis: Insights from petrogenesis of the Miocene Langkazi leucogranite and its dioritic enclaves. *Lithos*, *264*, 125–140. https://doi.org/10.1016/j.lithos.2016.08.019
Zhu, B., Zhang, H.-F., Zhao, X.-M., & He, Y.-S. (2016). Iron isotope fractionation during skarn-type alteration: Implications for metal source in the Han-Xing iron skarn deposit. *Ore Geology Reviews*, *74*, 139–150. https://doi.org/10.1016/j.oregeorev.2015.11.001
Zhu, C., Lu, W., He, Y., Ke, S., Wu, H., & Zhang, L. (2018). Iron isotopic analyses of geological reference materials on MC-ICP-MS with instrumental mass bias corrected by three independent methods. *Acta Geochimica*, *37*(5), 691–700. https://doi.org/10.1007/s11631-018-0284-5
Zhu, D. C., Wang, Q., Zhao, Z. D., Chung, S. L., Cawood, P. A., Niu, Y., et al. (2015). Magmatic record of India-Asia collision. *Scientific Reports*, *5*, 14289. https://doi.org/10.1038/srep14289

References From the Supporting Information

Boynton, W. V. (1984). Cosmochemistry of the rare earth elements: Meteorite studies. *Developments in geochemistry*, *2*, 63–114. https://doi.org/10.1016/B978-0-444-42148-7.50008-3
Liu, Z.-C., Wu, F.-Y., Qiu, Z.-L., Wang, J.-G., Liu, X.-C., Ji, W.-Q., & Liu, C.-Z. (2017). Leucogranite geochronological constraints on the termination of the South Tibetan Detachment in eastern Himalaya. *Tectonophysics*, *721*, 106–122. https://doi.org/10.1016/j.tecto.2017.08.019
Schärer, U., Xu, R.-H., & Allègre, C. J. (1986). U-(Th)-Pb systematics and ages of Himalayan leucogranites, South Tibet. *Earth and Planetary Science Letters*, *77*(1), 35–48. https://doi.org/10.1016/0012-821X(86)90130-5

Sun, S. s., & McDonough, W. F. (1989). Chemical and isotopic systematics of oceanic basalts: Implications for mantle composition and processes. *Geological Society, London, Special Publications*, *42*(1), 313–345. https://doi.org/10.1144/gsl.sp.1989.042.01.19

Watson, E. B., & Harrison, T. M. (1983). Zircon saturation revisited: Temperature and composition effects in a variety of crustal magma types. *Earth and Planetary Science Letters*, *64*(2), 295–304. https://doi.org/10.1016/0012-821X(83)90211-X

Wu, C., Nelson, K., Wortman, G., Samson, S. D., Yue, Y., Li, J., et al. (1998). Yadong cross structure and South Tibetan Detachment in the east central Himalaya (89°–90°E). *Tectonics*, *17*(1), 28–45. https://doi.org/10.1029/97TC03386

Yu, J. J., Zeng, L. S., Liu, J., Gao, L. E., & Xie, K. J. (2011). Early Miocene leucogranites in Dinggye area, southern Tibet: Formation mechanism and tectonic implications. *Acta Petrologica Sinica*, *27*(7), 1961–1972.